Available online at www.sciencedirect.com
SCIENCE DIRECT®
Journal of Computational Physics 214 (2006) 137–170
JOURNAL OF COMPUTATIONAL PHYSICS
www.elsevier.com/locate/jcp

A sequel to AUSM, Part II: AUSM$^+$-up for all speeds

Meng-Sing Liou *

Turbomachinery and Propulsion Systems Division, NASA Glenn Research Center, MS 5-11, 21000 Brookpark Road, Cleveland, OH 44135-3191, United States

Received 4 February 2005; received in revised form 12 September 2005; accepted 14 September 2005
Available online 3 February 2006

Abstract

In this paper, we present ideas and procedure to extend the AUSM-family schemes to solve flows at all speed regimes. To achieve this, we first focus on the theoretical development for the low Mach number limit. Specifically, we employ asymptotic analysis to formally derive proper scalings for the numerical fluxes in the limit of small Mach number. The resulting new scheme is shown to be simple and remarkably improved from previous schemes in robustness and accuracy. The convergence rate is shown to be independent of Mach number in the low Mach number regime up to $M_\infty = 0.5$, and it is also essentially constant in the transonic and supersonic regimes. Contrary to previous findings, the solution remains stable, even if no local preconditioning matrix is included in the time derivative term, albeit a different convergence history may occur. Moreover, the new scheme is demonstrated to be accurate against analytical and experimental results. In summary, the new scheme, named AUSM$^+$-up, improves over previous versions and eradicates fails found therein.

PACS: 47.11.+j; 47.40−x; 02.60Cb; 02.70.c

Keywords: Upwind scheme; Low Mach number; AUSM scheme; AUSM$^+$-up; Positivity; Entropy-satisfying; Carbuncle phenomenon; Euler and Navier–Stokes equations

1. Introduction

Today, computational fluid dynamics (CFD) codes are becoming a commodity used regularly for engineering analysis and even in the design process. Commercial codes have now been steadily employed, not only in industry but also in academia and government laboratories. CFD has been viewed by some as a matured discipline, thus requiring no further development. This view is further reinforced by the rapid advancement of ever faster and larger-memory computer processors, making computation of complex geometry and flow physics tractable and affordable. Hence, CFD no longer belongs to experts, but in fact is practiced largely by generalists. It is arguable that this advancement should be credited to those experts who have devoted

* Tel.: +1 216 433 5855; fax: +1 216 433 5802.
E-mail address: MENG-SING.LIOU@grc.nasa.gov.

0021-9991/$ - see front matter
doi:10.1016/j.jcp.2005.09.020

considerable efforts worrying about various facets of a numerical solution, such as accuracy, efficiency, stability, turbulence modeling, grid generation, etc.

As the usage of CFD becomes increasingly routine, it becomes even more prudent that attention is paid to developing a numerical scheme that is reliable for as wide a range of applications as physical modelings in the codes allow. Hence, we will emphasize the importance of reliability of computed solutions, which is a direct consequence of reliable numerical schemes and physical modelings. Here, reliability in this paper implies robustness, accuracy, and generality. In other words, the numerical scheme must be able to yield stable and accurate solutions under various flow conditions. Also, as the regime of applicability is extended, e.g., to different sets of conservation laws, stability and accuracy should still be maintained. We shall describe in this paper our recent effort towards attaining a reliable general numerical flux function.

One of the important extensions is to allow the application of the existing compressible flow codes to reliably predict low speed flows. It is well known that two major deficiencies occur when using a standard compressible code to calculate low speed flows: (1) extremely slow or stalled convergence and (2) grossly inaccurate solutions. These two phenomena are not related because the first one originates at the continuum level and is tied to the form of governing equations being solved, irrespective of the spatial discretization schemes used. However, the second deficiency is inherently tied to the flux scheme employed and is the subject of this paper.

In the 1990s, important developments have been made, such as those by Turkel [1], Choi and Merkle [2], Weiss and Smith [3] and Van Leer et al. [4], to devise a local preconditioner to alter the characteristics of the governing equations. In these cited studies, both the central differencing and the Roe schemes [5] have been used in the spatial discretization. Modifications of the AUSM-family schemes have also been proposed, resulting in a host of successful applications to not only low Mach flows [6–10], but also to multi-phase flows [11–14]. Among these studies, an interesting concept, so-called numerical speed of sound [8], was employed to conveniently rewrite the AUSM-family flux formulas. Despite successes in practice, the pressure split function reveals a discontinuity at $M = 0$ unless a cut-off Mach number was included. Although this parameter was also used in all of the preconditioners mentioned above, it is nevertheless desirable to have this parameter as small as the characteristic value in the flow, such as the free stream Mach number, without being limited to a preset value.

Another objective of the present investigation is to enhance the robustness of the previous AUSM$^+$ so that the convergence rate of calculations is independent of Mach numbers for low speed flows. And for other flow speed regimes, the convergence rate should remain at least as good. Moreover, the solution accuracy should be maintained for all speed ranges.

To achieve these objectives, we will derive a new scheme employing the asymptotic analysis under the limit of $M \to 0$.

The paper is organized as follows. We will begin by reviewing the existing AUSM schemes and their capabilities and shortcomings, thereby providing the motivation of the present study. Then, we describe in detail the development of the new scheme, called AUSM$^+$-up, and demonstrate its advantageous features with a series of benchmark problems. Next, to extend the capabilities to the low Mach number regime, asymptotic analysis is employed to derive proper scaling and final flux formulas. Finally, the efficacy of the new scheme is demonstrated for various types of problems, along with comparisons against theoretical and experimental results.

2. Development of a new AUSM numerical flux: AUSM$^+$-up

Our experiences have indicated that the key to achieve the above intended goals lies in the design of the inviscid fluxes.[1] Hence, let us begin by considering the inviscid equations written in vector form

$$\mathbf{Q}_t + \nabla \cdot \mathbf{F} = 0, \tag{1}$$

where $\mathbf{Q}$ and $\mathbf{F}$ are the vectors of usual conservative variables and inviscid fluxes, respectively.

[1] It is understood that the ultimate test of the scheme's capability will be done on the Navier–Stokes equations.

It is sufficient to consider only the 1D flux for now, but the extension to multi-dimensions follows the standard procedure of direction splitting. Hence, we shall take $\mathbf{Q} = (\rho, \rho u, \rho E)^{\mathrm{T}}$ and $\mathbf{F} = (\rho u, \rho u^2 + p, \rho u\, H)^{\mathrm{T}}$ and perfect gas.

The extension to other system of conservation laws can also be made, for example, for the two-fluid multiphase flow equations [14].

Before describing the new development for the AUSM-family schemes, it is instructive to first review its most current version.

As a first step common in all AUSM schemes, the inviscid flux is explicitly split into *convective* and *pressure* fluxes:

$$\mathbf{F} = \mathbf{F}^{(c)} + \mathbf{P} = \dot{m}\vec{\psi} + \mathbf{P}. \tag{2}$$

It is interesting to note that the convective flux comprises a common *scalar* mass flux $\dot{m}$, but having the sense of flow direction, for the entire system of conservation laws and a vector quantity $\vec{\psi}$ that is convected by $\dot{m}$, in which

$$\dot{m} = \rho u, \quad \vec{\psi} = (1, u, H)^{\mathrm{T}}. \tag{3}$$

The pressure flux contains only the pressure term,

$$\vec{\mathbf{P}} = (0, p, 0)^{\mathrm{T}}. \tag{4}$$

It is possible to write a numerical flux, mimicking the expression at the continuum level Eq. (2), in terms of a common mass flux,

$$\mathbf{f}_{1/2} = \dot{m}_{1/2}\vec{\psi}_{\mathrm{L/R}} + \mathbf{p}_{1/2}, \tag{5}$$

where $\vec{\psi}_{\mathrm{L/R}}$ will be determined in a simple upwind fashion,

$$\vec{\psi}_{\mathrm{L/R}} = \begin{cases} \vec{\psi}_{\mathrm{L}} & \text{if } \dot{m}_{1/2} > 0, \\ \vec{\psi}_{\mathrm{R}} & \text{otherwise}, \end{cases} \tag{6}$$

Clearly, the main tasks are to define the mass and pressure fluxes, $\dot{m}_{1/2}$ and $p_{1/2}$, which shall be described in detail, respectively, in this paper.

First, we shall digress briefly to discuss motivations of this study. Notwithstanding several good attributes found in the AUSM [15] and AUSM^{+} schemes [16], the single most notable deficiency has been the pressure oscillations observed along the grid direction in which there exists a very small velocity component. An example is in the direction normal to a boundary layer. Fig. 1 shows the pressure distribution of two colliding streams, between which a stagnant region immediately forms and expands with time. Overshoots appear at this stagnant region, precisely because of the lack of a dissipative mechanism in the pressure field.

This can be remedied with two approaches. Previously, we viewed it as a problem pertaining to the low Mach number flow and hence solved the problem by introducing the concept of numerical speed of sound (see [7,8]) such that the Mach numbers are rescaled to become on the order of unity over the range of subsonic speeds. This approach in the framework of AUSM schemes overcomes, in one formulation, two problems: (1)

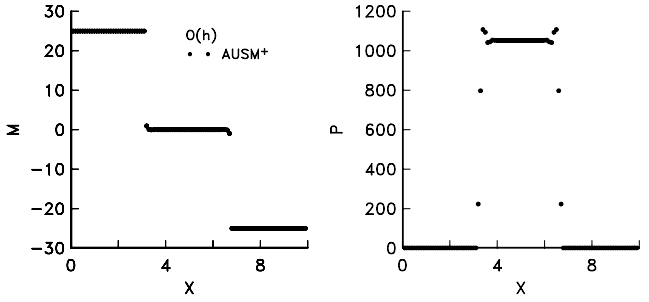

Fig. 1. Colliding shocks problem, $M_{\mathrm{L}} = -M_{\mathrm{R}} = 25$.

removal of pressure oscillations in the low speed regions, even when the flow speed in the bulk of domain may not be small and (2) extension of compressible flow formulation to solving flows where the entire region is at low Mach number.

The other approach is what we propose in this paper. The aim is to tackle the pressure-oscillations problem at the outset, irrespective of whether the flow speed is low. Then we will deal with the specific issues associated with low speed separately. This approach has the advantages of being simpler and having a basic scheme free of these oscillations at all speeds.

2.1. Mass flux

The mass flux at the interface denoted by subscript "1/2" has the form of

$$\dot{m}_{1/2} = u_{1/2}\rho_{\mathrm{L/R}} = a_{1/2}M_{1/2}\rho_{\mathrm{L/R}}, \tag{7}$$

where $u_{1/2}$ is the convective velocity and $\rho_{\mathrm{L/R}}$ is the density convected by $u_{1/2}$. The cell interface straddles two neighboring cells labeled by subscripts "L" and "R", respectively, namely to the left and right of the interface. Since the convective flux is associated with the linear field of the system of conservation laws, the interface density is dictated by the direction of $u_{1/2}$ in accordance with the idea of upwinding (convecting). That is,

$$\rho_{\mathrm{L/R}} = \begin{cases} \rho_{\mathrm{L}} & \text{if } u_{1/2} > 0, \\ \rho_{\mathrm{R}} & \text{otherwise.} \end{cases} \tag{8}$$

It turns out more convenient to use Mach number as a working variable and $u_{1/2}$ will be expressed in terms of polynomial functions of eigenvalues $M \pm 1$ associated with the nonlinear fields so that upwind switching can be automatically formulated at the sonic condition $M = \pm 1$. Thus, rewriting the above equation gives

$$\dot{m}_{1/2} = a_{1/2}M_{1/2}\begin{cases} \rho_{\mathrm{L}} & \text{if } M_{1/2} > 0, \\ \rho_{\mathrm{R}} & \text{otherwise.} \end{cases} \tag{9}$$

Clearly, the next question is how to define the interface speed of sound $a_{1/2}$ and Mach number $M_{1/2}$. As will become evident later, there can be remarkable possibilities for the definition of the speed of sound $a_{1/2}$. Specially defined forms of $a_{1/2}$ can give additional features.

To properly scale the numerical dissipation with the flow speed, the concept of numerical speed of sound was proposed in [8], in which we expressed it conveniently in terms of a scaling function f_a as:

$$\tilde{a}_{1/2} = f_a(\bar{M}; M_{\mathrm{o}})a_{1/2}. \tag{10}$$

The scaling factor f_a was given several forms, e.g., the one derived from the local preconditioned system [1–3],

$$V.0: f_a(\bar{M}; M_{\mathrm{o}}) = \frac{[(1 - M_{\mathrm{o}}^2)^2\bar{M}^2 + 4M_{\mathrm{o}}^2]^{1/2}}{1 + M_{\mathrm{o}}^2}, \tag{11}$$

with the reference Mach number,

$$M_{\mathrm{o}}^2 = \min(1, \max(\bar{M}^2, M_{\mathrm{co}}^2)), \tag{12}$$

where the mean local Mach number and cut-off Mach number are

$$\bar{M}^2 = \tfrac{1}{2}(M_{\mathrm{L}}^2 + M_{\mathrm{R}}^2) \quad \text{and} \quad M_{\mathrm{co}} = \kappa M_{\infty}, \ \kappa = \mathrm{O}(1). \tag{13}$$

The cut-off parameter M_{co} is nominally specified as $\mathrm{O}(M_{\infty})$ and should avoid becoming zero, which could lead to a floating point error. For a problem where no obvious representative Mach number can be identified, such as the shock tube problem, other characteristic parameters must be introduced.

We remark that it is not necessary to express the scaling factor with Eq. (11), so long as similar qualitative properties are maintained. In fact, a simpler form is possible,

$$V.1: f_a(M_{\mathrm{o}}) = M_{\mathrm{o}}(2 - M_{\mathrm{o}}) \geqslant 0 \approx 2M_{\mathrm{o}}, \quad \text{as } M_{\mathrm{o}} \to 0. \tag{14}$$

The behavior of these two formulas is displayed in Fig. 2. The effect of including the cut-off number is seen to introduce a non-zero f_a at $M = 0$. Since both formulas behave quite similarly and we found little differences of

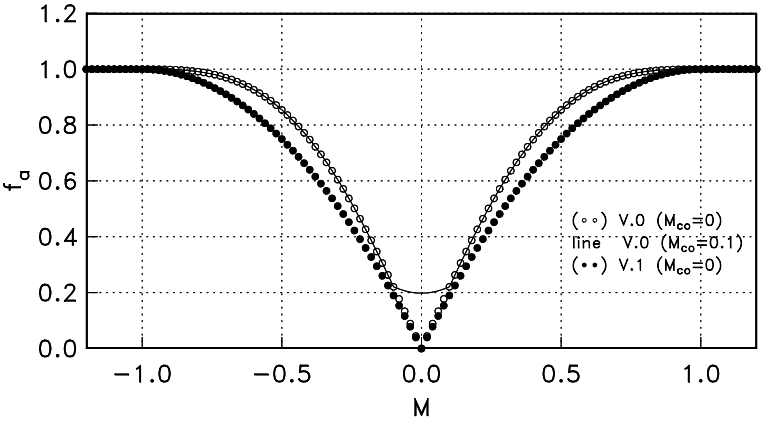

Fig. 2. Scaling functions used in the numerical speed of sound, using Eqs. (11) and (14).

their effects on the convergence rate and accuracy, Eq. (14) will be used, because of its simplicity, in all calculations presented in this paper.

Utilizing the numerical speed of sound $\tilde{a}_{1/2}$, a pair of "left" and "right" Mach numbers can be defined accordingly,

$$\tilde{M}_{\mathrm{L/R}} = \frac{u_{\mathrm{L/R}}}{\tilde{a}_{1/2}} = \frac{M_{\mathrm{L/R}}}{f_a}. \tag{15}$$

They would be used as "working variables" in the split functions of Mach number and pressure that will be given later. For convenience, this version is denoted as AUSM$^+$-a, because of the central role played by $\tilde{a}_{1/2}$. This pre-processing of Mach numbers has been shown to be effective in achieving an all-speed formulation of the AUSM-family schemes [6–12].

However, current effort is aimed at making the procedure simpler and more robust, while simultaneously improving its accuracy. A main objective is to eliminate the singularity caused by the division by f_a if it were allowed to become zero. Hence we shall abandon the use of $\tilde{a}$ entirely and find another way to attain desired features. We shall begin by eliminating the step of pre-processing Mach numbers and simply use the unscaled interface speed of sound to define $M_{\mathrm{L/R}}$,

$$M_{\mathrm{L/R}} = \frac{u_{\mathrm{L/R}}}{a_{1/2}}, \tag{16}$$

as the working variables in the scheme.

We can now set the interface Mach number in terms of M_{L} and M_{R} as:

$$M_{1/2} = \mathscr{M}^+_{(m)}(M_{\mathrm{L}}) + \mathscr{M}^-_{(m)}(M_{\mathrm{R}}) + M_p. \tag{17}$$

The split Mach numbers $\mathscr{M}^\pm_{(m)}$ are polynomial functions of degree m (= 1,2,4), as given in [16]:

$$\mathscr{M}^\pm_{(1)}(M) = \tfrac{1}{2}(M \pm |M|), \tag{18}$$

$$\mathscr{M}^\pm_{(2)}(M) = \pm\tfrac{1}{4}(M \pm 1)^2 \tag{19}$$

and

$$\mathscr{M}^\pm_{(4)}(M) = \begin{cases} \mathscr{M}^\pm_{(1)} & \text{if } |M| \geqslant 1, \\ \mathscr{M}^\pm_{(2)}(1 \mp 16\beta\mathscr{M}^\mp_{(2)}) & \text{otherwise.} \end{cases} \tag{20}$$

The pressure diffusion term M_p, introduced to enhance calculations of low Mach number or multi-phase flow, is defined to be:

$$M_p = -K_p \max(1 - \sigma\bar{M}^2, 0)\frac{p_{\mathrm{R}} - p_{\mathrm{L}}}{\rho_{1/2}a^2_{1/2}}, \quad \sigma \leqslant 1, \ \rho_{1/2} = (\rho_{\mathrm{L}} + \rho_{\mathrm{R}})/2 \tag{21}$$

with $0 \leqslant K_p \leqslant 1$. The factor $\max(1-\sigma\bar{M}^2) \geqslant 0$ is introduced to replace a similar function $\Delta\mathscr{M}$ used in the previous low Mach number formulations [7,8],

$$\Delta\mathscr{M} = [\mathscr{M}^+_{(4)} - \mathscr{M}^+_{(1)}](M_L) - [\mathscr{M}^-_{(4)} - \mathscr{M}^-_{(1)}](M_R) \geqslant 0. \tag{22}$$

Both functions behave qualitatively in a similar manner. They monotonically increase from zero as $|M| \geqslant 1$ to a maximum value at $M = 0$, as shown in Fig. 3 (the difference in magnitude is immaterial because it can be absorbed in the co-efficient K_p). Since the current one is simpler, it has been used in all calculations throughout this paper. The factor $\max(1-\sigma\bar{M}^2, 0)$ becomes activated only in the region of $M^2 \leqslant 1/\sigma$ with $\sigma \leqslant 1$.

We remark that this pressure diffusion term may not provide sufficient dissipation at low Mach number because $\Delta p = p_R - p_L$ will be small and in fact is $O(M^2) \ll 1$. Hence, a close examination of this aspect is required. It is a main focus of this investigation, as will be shown in the next section on Extension for All Speeds, in which we shall utilize the asymptotic analysis to derive a proper scaling for M_p.

2.2. Pressure flux

In all the AUSM-family schemes, a general interface pressure formula [16] is used as a starting point,

$$p_{1/2} = \mathscr{P}^+_{(n)}(M_L)p_L + \mathscr{P}^-_{(n)}(M_R)p_R, \tag{23}$$

where $n = 1, 3$, or 5 corresponds to the degree of the polynomials $\mathscr{P}^{\pm}$, as in $\mathscr{M}^{\pm}$. The fifth degree polynomials are preferred because they are found to yield more accurate solutions. They are also expressed in terms of split Mach number functions, as given by

$$\mathscr{P}^{\pm}_{(5)}(M) = \begin{cases} \frac{1}{M}\mathscr{M}^{\pm}_{(1)} & \text{if } |M| \geqslant 1, \\ \mathscr{M}^{\pm}_{(2)}[(\pm 2 - M) \mp 16\alpha M \mathscr{M}^{\mp}_{(2)}] & \text{otherwise.} \end{cases} \tag{24}$$

Notice that the pair of parameters α, β were set previously to be, respectively $(3/16, 1/8)$ under the conditions described in [16]. In next section, we will re-examine the definition of α and β with additional requirements for the low Mach number flow.

The above pressure flux was recently modified [20] by adding a velocity difference (diffusion) term p_u, similar to the interface Mach number given in Eq. (17),

$$p_{1/2} = \mathscr{P}^+_{(5)}(M_L)p_L + \mathscr{P}^-_{(5)}(M_R)p_R + p_u, \tag{25}$$

where

$$p_u = -K_u\mathscr{P}^+_{(5)}(M_L)\mathscr{P}^-_{(5)}(M_R)(\rho_L + \rho_R)a_{1/2}(u_R - u_L), \tag{26}$$

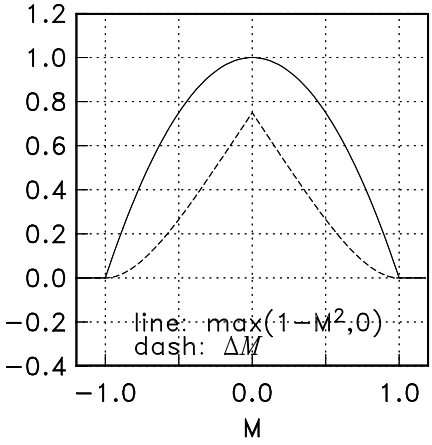

Fig. 3. Mach-number factors in $M_p(\sigma = 1)$.

and the coefficient $0 \leqslant K_u \leqslant 1$. It is noteworthy that the added velocity diffusion term was inspired by approximating the characteristic relations $\mathrm{d}p \pm \rho a\,\mathrm{d}u = 0$ to yield,

$$p_{1/2} = \tfrac{1}{2}(p_L + p_R) - \tfrac{1}{2}(\rho a)_{1/2}(u_R - u_L) \tag{27}$$

for M_L, $M_R \leqslant 1$. The coefficient $\mathscr{P}^+_{(5)}(M_L)\mathscr{P}^-_{(5)}(M_R)$ simply switches off p_u as the flow becomes supersonic, resulting in one-sided upwinding. It is of interest to note that several members of the AUSM-family also have a similar term, e.g., AUSMDV [25], AUSMPW$^+$ [17] and LDFSS [7].

We call this version AUSM$^+$-u where the suffix "u" is used to indicate that the velocity diffusion term is included. By the same token, the scheme reads AUSM$^+$-up when M_p is also included in Eq. (17). In other words, what is added onto the AUSM$^+$ [16] is simply both the M_p and p_u terms to render it AUSM$^+$-up. The AUSM$^+$-up is also denoted as the basic scheme in this paper. In Section 3, we shall add a further development to make it uniformly valid for all speed regimes and some other features.

Let us first validate the efficacy of the basic scheme before turning to the development for low Mach number flows. For applications of the basic scheme to the solution of multi-phase multi-fluid equations, see [14]. In this section, all results are of $O(\Delta x)$ accurate unless stated otherwise.

2.3. Choice of interface speed of sound $a_{1/2}$

2.3.1. Shock resolution

Similar to the AUSM$^+$ scheme [16], it is also possible for the basic scheme to find an interface speed of sound $a_{1/2}$ such that a normal shock can be exactly resolved between two discontinuous states, even when both M_p and p_u are included. Interestingly, the same formula is valid here as well, i.e.,

$$a_{1/2} = \min(\hat{a}_L, \hat{a}_R), \quad \text{where } \hat{a} = a^{*2}/\max(a^*, |u|). \tag{28}$$

Here, a^* is the critical speed of sound evaluated when the local Mach number is unity. In the case of perfect gas, this can be expressed in terms of total enthalpy,

$$a^{*2} = \frac{2(\gamma - 1)}{\gamma + 1} H_t. \tag{29}$$

The result displayed in Fig. 4 demonstrates that a stationary shock is exactly preserved.

2.3.2. Entropy-satisfying property

Because of this exactness property of resolving a shock, no distinction between a (compression) shock or an entropy-violating expansion shock can be made, as displayed in Fig. 5, where both the speed of sound given in

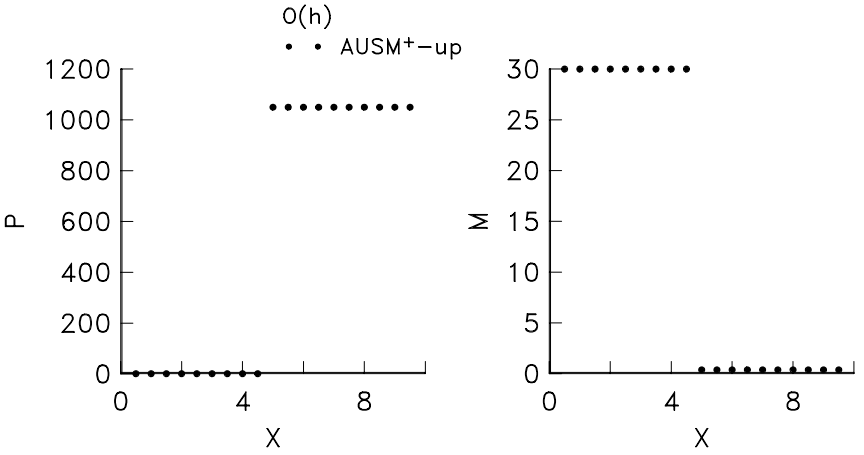

Fig. 4. Exact shock capturing.

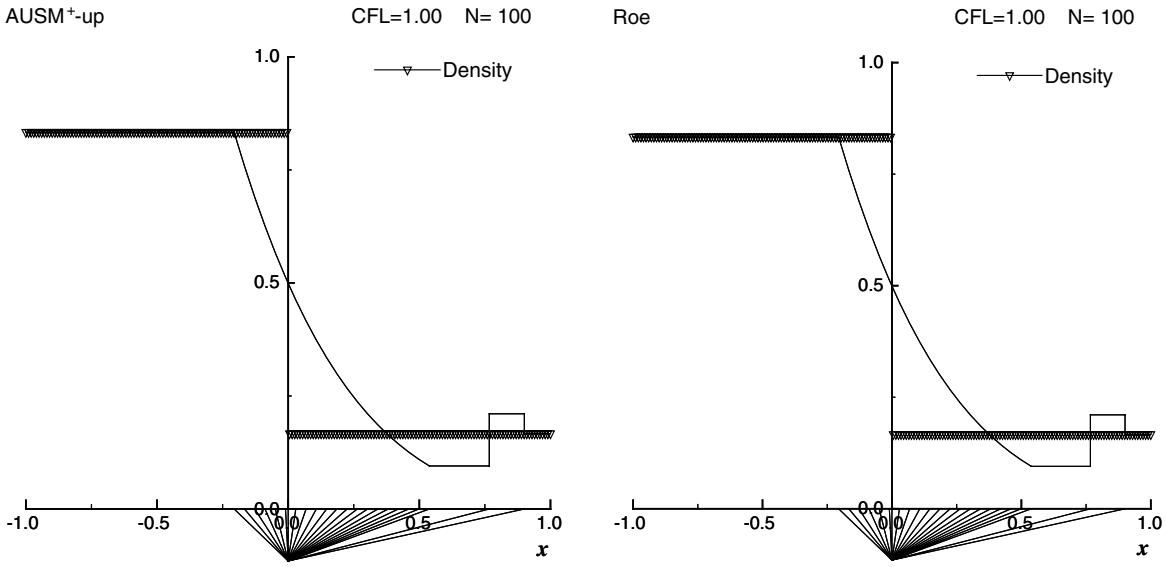

Fig. 5. Inverse shock problem showing violation of the entropy condition. Left: Eq. (28); Right: Roe splitting.

Eq. (28) and the Roe flux splitting yield an expansion shock, instead of the entropy-satisfying exact solution shown with the solid line.

Interestingly, a slight modification of Eq. (28) will just cure the problem by simply incorporating the information of flow direction, which can be readily accomplished by inserting a "−" sign in u_R,

$$\hat{a}_L = a^{*2}/\max(a^*, u_L), \quad \hat{a}_R = a^{*2}/\max(a^*, -u_R). \tag{30}$$

The initial entropy-violating jump states now turn into a smooth expanding flow, as seen in Fig. 6. It is noteworthy that the basic scheme, AUSM$^+$-up, gives a smoother transition through the sonic point than the Godunov's exact Riemann solver. The same advantageous feature also shows up in the solution of a shock diffracting around a sharp corner (Fig. 15, shown later in this section).

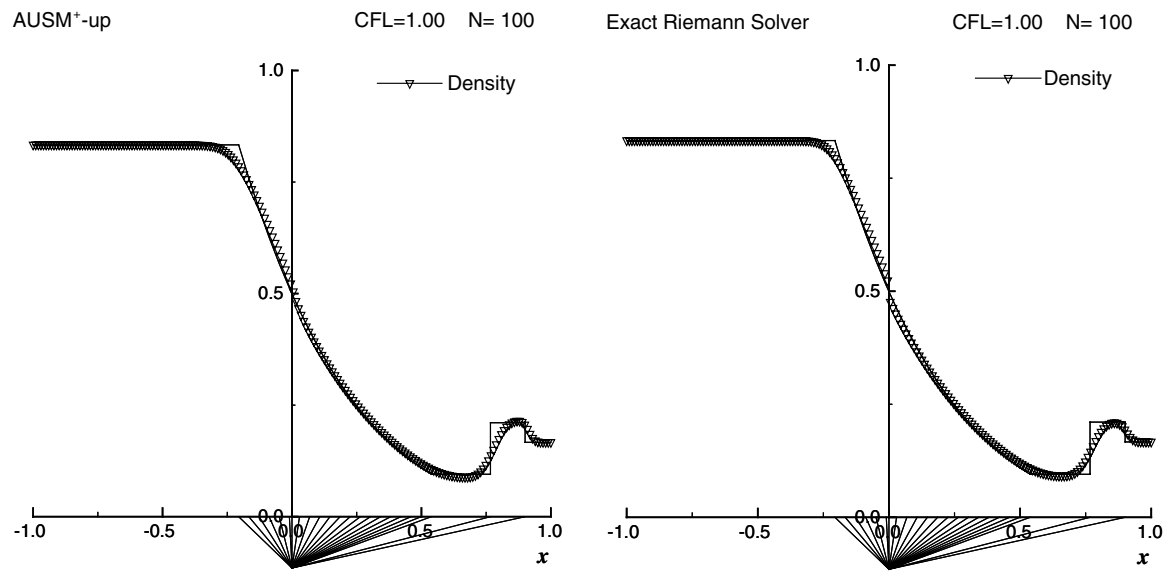

Fig. 6. Inverse shock problem showing the entropy-satisfying property. Left: Eq. (30); Right: Godunov method.

2.4. Additional features of the basic scheme

In what follows immediately we will examine a series of 1D problems with different characteristics. The 1D benchmark problems are of interest because one can precisely devise a problem mimicking a single or multiple events occurring in more complex 3D problems. Hence, one can get a clear insight into the mechanism failing a numerical scheme.

2.4.1. Monotonicity

First, we check on the solution of two colliding shocks moving at $M = 25$. As we saw in Fig. 1, the previous AUSM$^+$ scheme yielded overshoots behind the shock. Now, we see in Fig. 7 that the current AUSM$^+$-up completely removes the overshoots and gives monotonic profiles. The Roe splitting results are also included for comparison in which very slight overshoots are observed at the shoulder of the pressure profiles.

2.4.2. Positivity property

A test on the robustness of a scheme is the receding flow (vacuum) problem in which two parts of the fluid begin to recede from each other at $t = 0$, subsequently resulting in a drop in pressure and density in the middle, see Fig. 8. This is relevant to calculating rapid rarefaction seen in some flow problems, e.g., around a sharp corner. The Roe scheme is known to fail in this test. The capability to preserve positivity in pressure and density in this vacuum problem has been demonstrated with the previous AUSM schemes; this new scheme again maintains this capability.

2.4.3. Sonic point resolution

Now we examine a flow accelerating through the sonic point; its results are given in Fig. 9. The Roe splitting yields a discontinuous solution at the sonic point and the van Leer splitting [21] gives a slight glitch near the sonic point. However, the current basic scheme yields a smooth transition through the sonic point if the

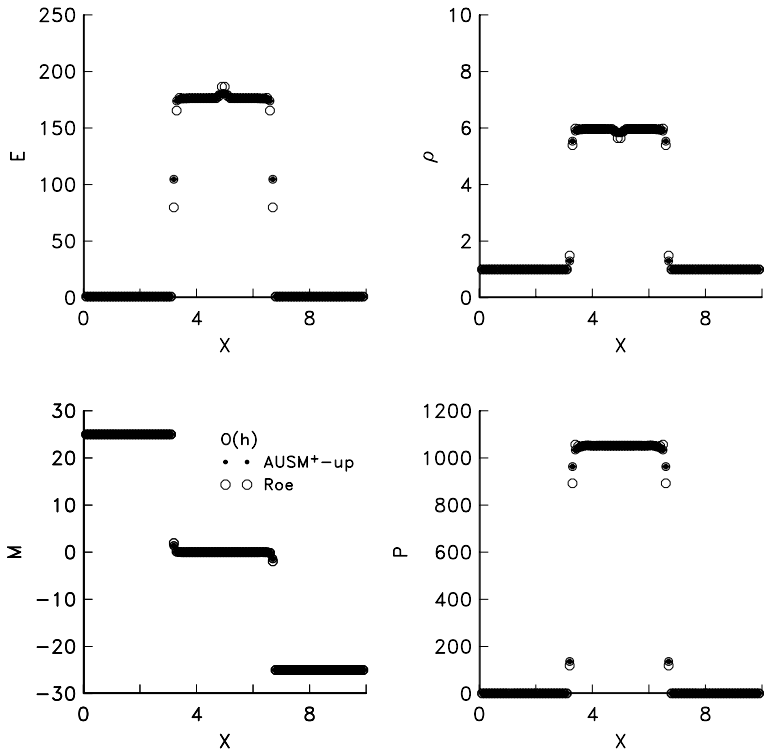

Fig. 7. Colliding shocks problem, $M_L = -M_R = 25$; comparison of results by the Roe splitting and AUSM$^+$-up.

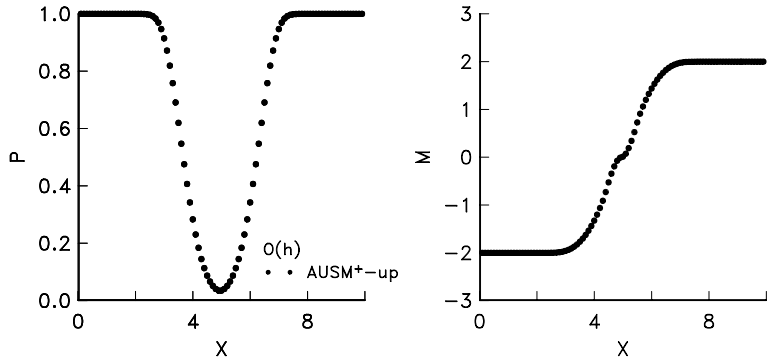

Fig. 8. Receding flow (vacuum) problem, $M_L = -M_R = -2$.

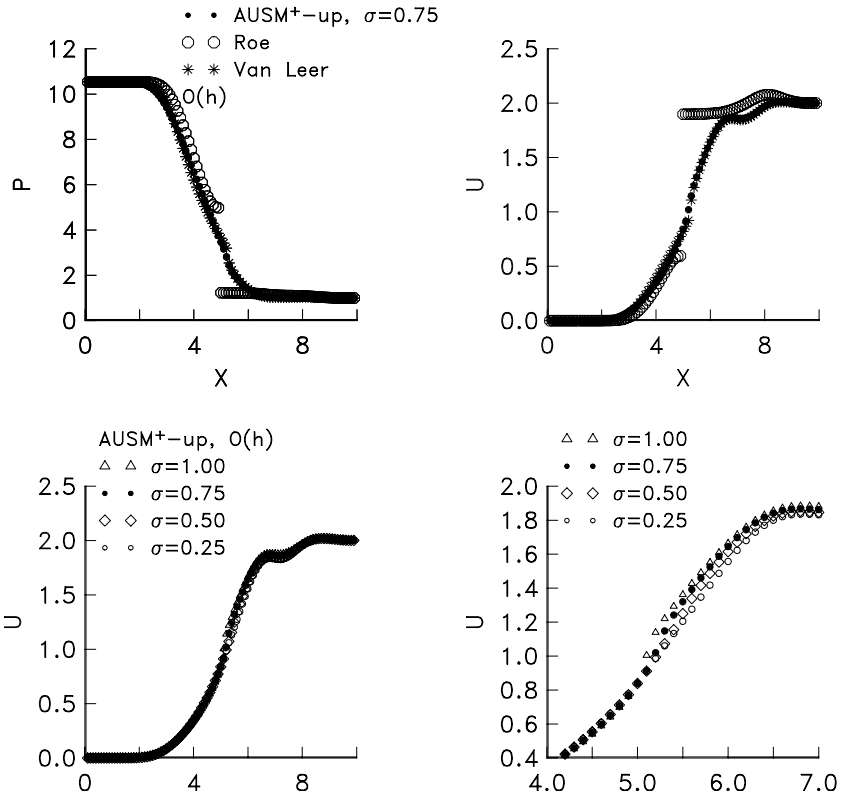

Fig. 9. Expansion through sonic point showing the results by the Roe and van Leer splittings and AUSM$^+$-up. A magnified view of the effect of σ on the solution is given in the lower right figure.

parameter σ in Eq. (21) is chosen to be smaller than unity, see the enlarged view of the velocity distribution near $x = 5.0$. Results of using different values of σ are also shown in Fig. 9. It is clear that the smaller σ becomes, the smoother the result is. Note that σ becomes effective only in the supersonic region, where $1 \leqslant M^2 \leqslant 1/\sigma$. The results show that it is just a simple fix for this sonic point problem by allowing the parameter $\sigma < 1$. It is noted that the author is unaware of any case that is effected in a fundamental way, i.e., resulting in a qualitatively different solution, by choosing a sensible range of values of σ, e.g., $1/4 \leqslant \sigma < 1$. A lower value of σ tends to make the supersonic region smoother. It is interesting to note that a lower bound of σ may be set by a requirement that the exact shock capturing property be preserved, namely

$$M_p = 0 \quad \forall \bar{M} \geqslant 1 \quad \Rightarrow \quad 1 - \sigma^* \bar{M}^2 = 0, \quad \sigma^* \leqslant \sigma \leqslant 1. \tag{31}$$

If $\bar{M}^2 = (M_L^2 + M_R^2)/2$ and using the Prandtl relation that is essential in achieving the exact shock capturing property [16], we get a simple analytical expression for σ^*,

$$\sigma^* = \frac{2}{1 + (M_L a_L / a_L^*)^4}. \tag{32}$$

Fig. 10 shows that this lower bound σ^* drops quickly as M_L increases. If the region activated by the factor $\max(1 - \sigma \bar{M}^2, 0)$ is to be narrowed, then a value close to one should be chosen.

2.4.4. Contact discontinuities: stationary and slowly moving

First, it is easy to show the exact property of the AUSM-family schemes for capturing a stationary contact discontinuity in which $\rho_L \neq \rho_R$, $u_L = u_R = 0$, $p_L = p_R = p$. The property of exactly capturing a contact discontinuity has been proved for AUSM$^+$ in [16] and it is easy to see that AUSM$^+$-up reduces to AUSM$^+$ because the additional terms M_p and p_u vanish accordingly. Next, we consider a slowly moving contact with the initial conditions [25]: $(\rho, p, u)_L = (1, 1, 0.3a_R)$, $(\rho, p, u)_R = (10, 1, 0.3a_R)$. Fig. 11 presents the pressure and density distribution in which a constant pressure and a sharp density jump are obtained across the contact.

2.4.5. Slowly impacting problem

Next, we shall consider the flow created by a slowly moving ($M = 0.001$) stream of fluid impacting on a fluid at rest. This case is studied with the initial conditions: $(\rho, p, u)_L = (1, 1, 0.001a_L)$, $(\rho, p, u)_R = (1, 1, 0)$. The comparison of results from the Roe splitting and AUSM$^+$-up against the exact solution is shown in

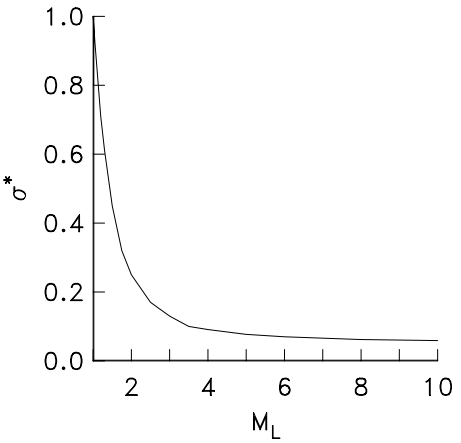

Fig. 10. Lower bound of σ vs. M_L.

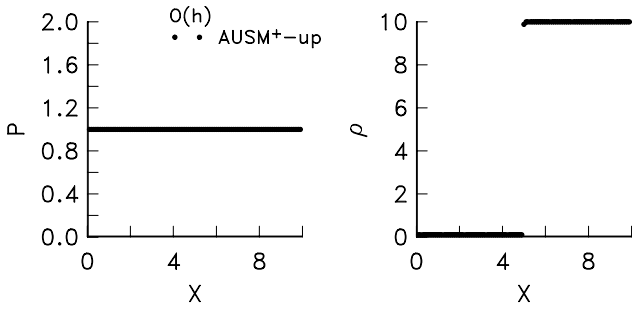

Fig. 11. Slowly moving contact.

Fig. 12. Here, the initial velocity jump is now separated by a middle region of constant properties. Results from the Roe splitting are clearly in error, on the order of 0.1 M.

2.4.6. Slowly moving shock discontinuity

Unlike the contact discontinuity problem, this one is about the nonlinear discontinuity field. Roberts [22] proposed a test problem to study numerical noises generated by a slowly moving shock with a speed much smaller than the acoustic speed. It is known that several upwind schemes (Godunov [23], Roe [5], and HLLE [24]) produce serious errors behind the shock [25]. Fig. 13 shows the comparison between solutions of the Godunov and AUSM$^+$-up schemes. The latter gives smoother profiles, with nearly constant strength of the linear and the two nonlinear waves behind the shock.

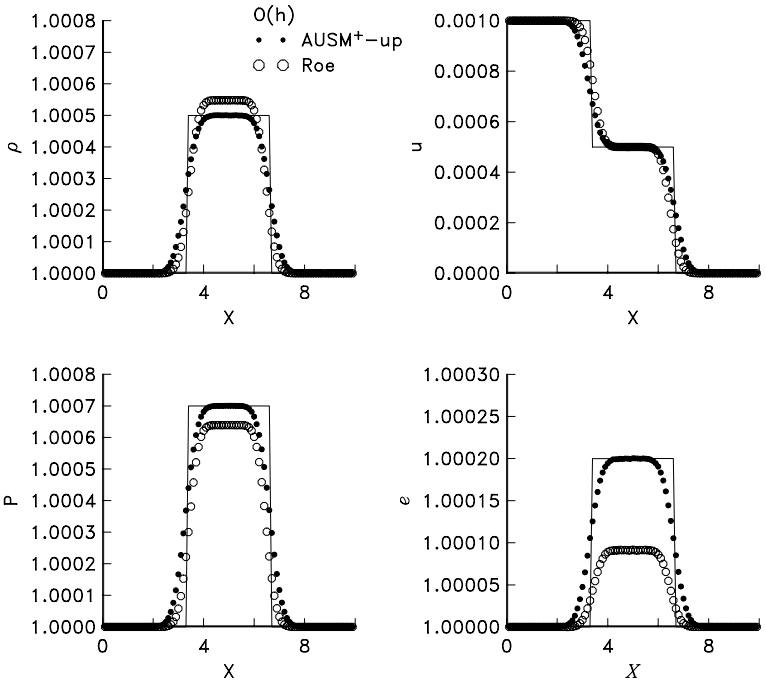

Fig. 12. Slowly impacting problem showing results by the Roe splitting and AUSM$^+$-up.

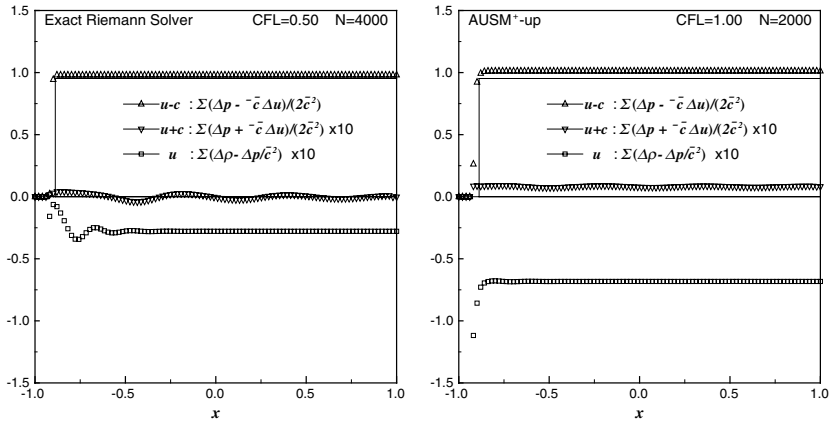

Fig. 13. Slowly moving shock problem. Left: exact Riemann solver; Right: AUSM$^+$-up.

2.4.7. Shock instability: carbuncle phenomenon

Next, we investigate the so-called shock instability problem [26], first proposed by Quirk [27], in which a plane shock wave is propagating along a channel of constant area. The grid at the mid-channel is perturbed alternately at odd and even points with a small magnitude. For a certain class of numerical schemes, this grid perturbation is sufficient to trigger numerical catastrophes, the so-called ''carbuncle phenomenon'', see discussion in [26] for details. In Fig. 14, we show the result from the current scheme, it is clearly free of any anomalies, maintaining a clean profile along the shock and a monotone distribution along the channel.

We now consider another problem investigated by Quirk [27], namely, the diffraction of a plane shock wave moving around a 90° corner, subsequently generating a series of complex shock diffraction, reflection, and interaction patterns. This test problem can reveal several unit anomalies discussed above. For examples, a scheme may produce shock instability at the vertical stem of the main shock or an entropy-violating expansion fan emanating from the corner. Fig. 15 shows the computed results on a 71×71 grid from the Godunov and

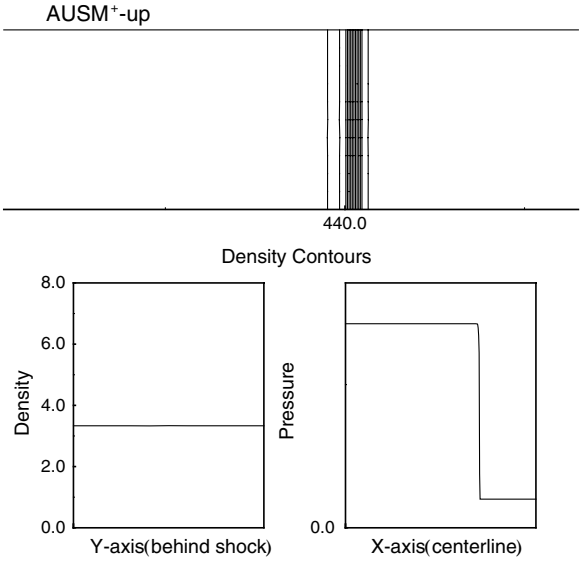

Fig. 14. Odd–even grid perturbation problem; CFL = 1, $p_R/p_L = 7.1$.

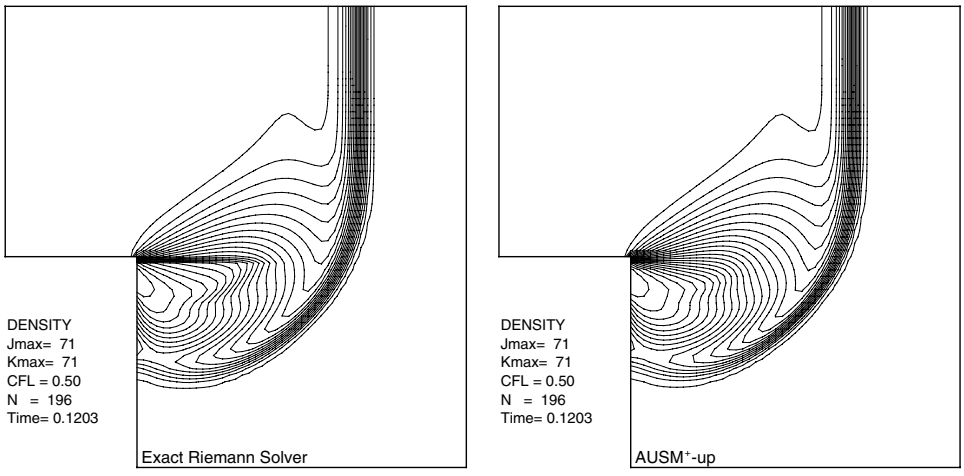

Fig. 15. Supersonic shock diffraction problem. Left: exact Riemann solver; Right: AUSM$^+$-up.

the basic schemes. The former produces a discontinuous expansion fan, while the latter yields a smooth divergent fan, indicating the satisfaction of the entropy condition.

A second-order accurate, fine grid solution shown in Fig. 16 was obtained on a 400×400 grid, with the minmod limiter, revealing rich flow features that were grossly smeared by the coarse-grid solution. The first-order accurate solution on this fine grid is also included for comparison; it completely smeared one of the internal shocks and the reflected shock emanating from the triple point. It is evident from this example that a higher-order accurate procedure is significantly useful. Grid-adaptive procedure was shown by Quirk [27] to yield more fine features.

It should be noted that the present scheme does include a pressure diffusion term in the mass flux, but no shock instability such as the carbuncle phenomenon has yet been detected. This, however, is not in conflict with the Conjecture suggested in [26] in which the condition with the pressure diffusion term is only stated as a necessary one for the shock instability to occur. Nevertheless, the fact that we have not observed this numerical anomaly in the solutions presented above does not mean it will never happen under any circumstances. However, it simply confirms the robustness of the present scheme.

3. Extension of AUSM$^+$-up for all speeds

As noted earlier, standard methods developed for compressible flows do not function properly when they are applied to low Mach number flows. They are beset by convergence and accuracy problems. The first problem is associated with the disparity of convective and acoustic speeds as $M \to 0$. The standard approach to rectify this problem is to modify the structure of eigenvalues at the continuum level through preconditioning of the time derivative term. The second problem is closely related to the method of discretization. As $M \to 0$, the pressure term is dominating the flow field, i.e., small perturbation in the pressure field results in zeroth-order changes in the velocity field. Hence, proper scaling of pressure differences must be reflected in the numerical scheme; otherwise, inaccuracy crops up and corrupts the solution.

While the concept of numerical speed of sound [8] mentioned earlier is intriguing and useful for dealing with the accuracy problem, it however introduces non-smoothness in the pressure split functions. A discontinuity appears, as shown in Fig. 17, at stagnation point $M = 0$ and is avoided only by the introduction of the cut-off Mach number M_{co} used in Eq. (12). However, this cut-off Mach number in practice is prevented from becoming too small by limiting it to a finite value, for example, by setting $M_{co} = \max(0.3, \frac{1}{2}M_\infty)$. The lower bound value of 0.3 is used conventionally in most works on low Mach number preconditioning, but it is also a good choice in the sense of Fig. 17, where the split functions become smooth when the value of 0.32 is used. In fact, this version of AUSM-family schemes has been used quite satisfactorily and reported in several publications,

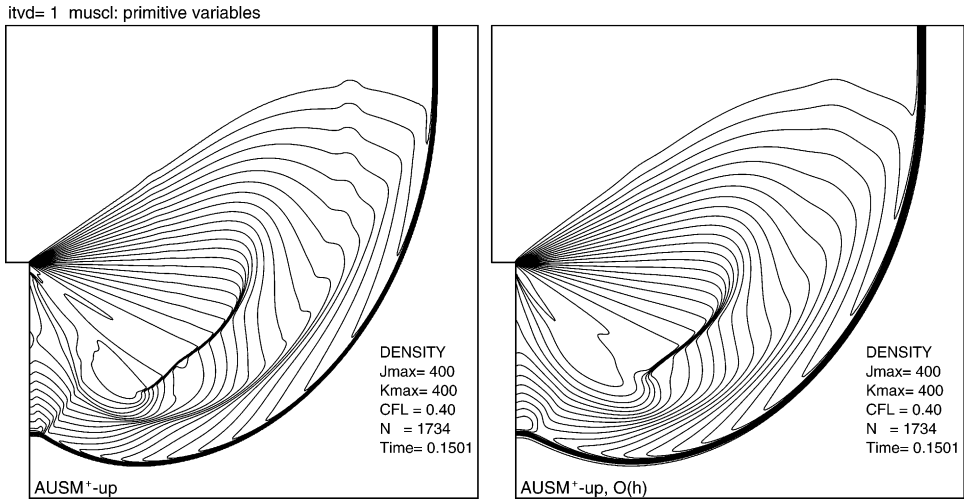

Fig. 16. Supersonic shock diffraction problem solved by AUSM$^+$-up on a fine gird of 400×400 points. Left: O(h^2); Right: O(h).

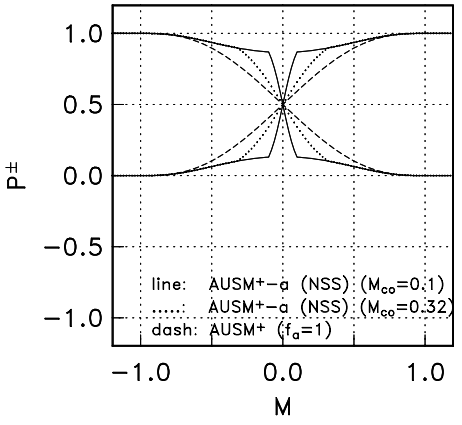

Fig. 17. Split pressure functions used in AUSM$^+$-a ($f_a(M, M_o(M_{co}))$) and AUSM$^+$ schemes ($f_a = 1$).

such as [6,8–10,13,11,20]. Nevertheless, it would be desirable if this somewhat arbitrary preset value can be avoided and M_{co} can be allowed as low as M_∞ may be, e.g., $M_{co} = O(M_\infty)$, rather than being bounded from below by 0.3.

To achieve this goal, we employed the analysis of asymptotic series expansion for low Mach number to derive proper scales required in the pressure and velocity diffusion terms.

3.1. Asymptotic analysis for low Mach number

One of the advantages unique to asymptotic analysis is that it reveals formally proper scalings as some parameters go to their limits. In this study, we follow [19] to derive the limits of the compressible inviscid equations as the Mach number vanishes. First, the equations are non-dimensionalized by appropriate reference quantities such that each non-dimensional variable remains of order unity. Denoting the reference quantities with a subscript "*" and the dimensional quantities with an "overbar", we select $(\bar{L}_*, \bar{U}_*)$ to non-dimensionalize $(\bar{t}, \vec{\bar{x}}, \vec{\bar{u}})$, and $(\bar{\rho}_*, \bar{a}_*^2)$ to non-dimensionalize the thermodynamic variables, $(\bar{p}, \bar{\rho}, \bar{e})$. Note that it is proper to choose $\bar{a}_*$ as a reference quantity for compressible flows since the speed of sound is related to the changes of $\bar{p}$ and $\bar{\rho}$.

There are two distinct time scales in low Mach number flows and they are characterized, respectively, by the convection speed $\bar{U}_*$ and speed of sound $\bar{a}_*$. They differ in fact by a factor of Mach number, $M_* = \bar{U}_*/\bar{a}_*$. Hence, two time limits can be formulated to consider slow and fast unsteady motions, see [18], for example. In this study, we are mainly concerned with the convergence behavior towards the steady-state solutions. In such situations, the convergence rate is mainly controlled by the slowest wave propagation. Consequently, the flow speed $\bar{U}_*$ is a rate-controlling factor and is chosen in the non-dimensionalization for the analysis of low Mach number flows.

The resulting non-dimensional equations become, if $M_* = \bar{U}_*/\bar{a}_*$,

$$\frac{\partial \rho}{\partial t} + \nabla \cdot \rho \vec{u} = 0, \tag{33}$$

$$\frac{\partial \rho \vec{u}}{\partial t} + \nabla \cdot \rho \vec{u}\vec{u} + \frac{1}{M_*^2} \nabla p = 0, \tag{34}$$

$$\frac{\partial \rho E}{\partial t} + \nabla \cdot \rho u H = 0. \tag{35}$$

Let us denote the vector of primitive variables by

$$\mathbf{Q} = [\rho, \vec{u}, p]^{\mathrm{T}}. \tag{36}$$

For $M_* \to 0$, we can seek solutions of the above systems via the following expansion of variables:

$$\mathbf{Q} = \mathbf{Q}^{(0)} + M_* \mathbf{Q}^{(1)} + M_*^2 \mathbf{Q}^{(2)} + \cdots \tag{37}$$

By substituting this expansion into the above-non-dimensional equations, it is easy to see that the first two leading equations describe variations of pressure only:

$$\nabla p^{(0)} = 0 \;\Rightarrow\; p^{(0)}(t) \tag{38}$$

and

$$\nabla p^{(1)} = 0 \;\Rightarrow\; p^{(1)}(t). \tag{39}$$

The other variables only begin to appear together with the second-order pressure $p^{(2)}$. Consequently, after some algebraic manipulations and deductions, we can summarize the following results.

From Eqs. (38) and (39), the pressure is constant in space up to and including the first order, $O(M_*)$. Hence, by absorbing $p^{(1)}$ into $p^{(0)}$, we have

$$p(\vec{x}, t) = p^{(0)}(t) + M_*^2 p^{(2)}(\vec{x}, t) + \cdots \tag{40}$$

The zeroth-order pressure changes only with time, indicating that the entire domain of interest is under compression or expansion simultaneously at the same rate.

Because $\rho E = \frac{p}{(\gamma-1)} + \frac{M_*^2}{2}|\vec{u}|^2 = \frac{p^{(0)}}{(\gamma-1)} + O(M_*^2)$, we find from the energy equation,

$$\frac{\mathrm{d}p^{(0)}}{\mathrm{d}t} + \gamma p^{(0)} \nabla \cdot \vec{u}^{(0)} = 0. \tag{41}$$

Integrating over the domain of interest Ω, we get

$$\frac{\mathrm{d}\ln p^{(0)}}{\mathrm{d}t} + \frac{\gamma}{|\Omega|} \int_{\partial\Omega} \vec{u}^{(0)}(\vec{x}, t) \cdot \vec{n}\, \mathrm{d}S = 0 \tag{42}$$

in which the Gauss theorem has been applied in the integral. This result implies that $p^{(0)}(t)$ can be obtained by only knowing the fluid velocity crossing the boundary of the domain together with a known initial value of $p^{(0)}(0)$.

The zeroth-order velocity, $\vec{u}^{(0)}(\vec{x}, t)$, is related to the second-order pressure via the momentum equation,

$$\frac{\partial \vec{u}^{(0)}}{\partial t} + \nabla \cdot \vec{u}^{(0)} \vec{u}^{(0)} + \frac{1}{\rho^{(0)}} \nabla p^{(2)} = 0. \tag{43}$$

The zeroth-order density follows from the continuity equation with the known $\vec{u}^{(0)}$,

$$\frac{\partial \rho^{(0)}}{\partial t} + \nabla \cdot \rho^{(0)} \vec{u}^{(0)} = 0. \tag{44}$$

As a result, the quantities $p^{(2)}$, $\rho^{(0)}$ and $\vec{u}^{(0)}$ have to be solved simultaneously, with appropriate boundary and initial conditions.

Consequently, we arrive at the following remarks:

R1. Since $p^{(0)}(t)$, this result is clearly not valid for the shock tube problems where the zeroth-order solution is not spatially constant. Hence, the numerical scheme developed for low Mach number situations is *not* suitable for the shock tube problems. In fact, the basic scheme given in the previous section should be used even though the flow speed in the entire domain may be very low, as in the cases of slowly moving contact/shock, see Figs. 11–13.

R2. Even though $p^{(0)}(t)$, the zeroth-order density and internal energy can be spatially varying, i.e., $\rho^{(0)}(\vec{x}, t)$, as clearly implied in Eq. (44). Moreover, this pressure $p^{(0)}(t)$ is decoupled from the equation of the state, it instead is determined from the energy equation with the constraint on the divergence of velocity. Therefore, acoustic waves are removed from the system of equations, as in the case of incompressible flows.

R3. The second-order pressure solution $p^{(2)}(\vec{x}, t)$ acts as a source to the convection of the zeroth-order velocity field. Hence, if a numerical method gives spatial fluctuations in pressure on the order of M_*, rather than M_*^2 in the low Mach number limit, then inaccurate solutions will develop in the form of $\vec{u}^{(0)}$, $\rho^{(0)}$ and $e^{(0)}$.

R4. As noted above, when the fast motion characterized by the speed of sound $\bar{a}_*$, instead of $\bar{U}_*$, is included, the time derivatives are decreased by a factor of M_* [18]. Hence, the first-order pressure fluctuation is now both time- and space-dependent, i.e., $p^{(1)}(\vec{x},t)$. As expected, this pressure is governed by the acoustic wave equation.

3.2. $AUSM^+$-up for all speeds

The objective of the present study is to develop a new scheme that is uniformly valid for all speed regimes. Let us now consider the basic scheme described earlier under the limit of vanishing Mach number. Again, define

$$M_{\mathrm{L/R}} = \frac{\bar{u}_{\mathrm{L/R}}}{\bar{a}_{1/2}} = \frac{\bar{U}_* u_{\mathrm{L/R}}}{\bar{a}_* a_{1/2}} = M_* \hat{M}_{\mathrm{L/R}}, \quad M_* = \frac{\bar{U}_*}{\bar{a}_*}, \quad \hat{M} = \frac{u}{a}. \tag{45}$$

Note that since u and a are O(1), hence $\hat{M} = \mathrm{O}(1)$ and $M_{\mathrm{L/R}} = \mathrm{O}(M_*)$. That is, for low Mach number flows, both M_* and $M_{\mathrm{L/R}} \to 0$. Now, using the split functions $\mathscr{M}^+_{(4)}(M_{\mathrm{L}})$ and $\mathscr{M}^-_{(4)}(M_{\mathrm{R}})$, we obtain expressions in the limit of $M_{\mathrm{L/R}} \to 0$,

$$M_{1/2} = \mathscr{M}^+_{(4)}(M_{\mathrm{L}}) + \mathscr{M}^-_{(4)}(M_{\mathrm{R}}) + M_p = \frac{1}{2}(M_{\mathrm{L}} + M_{\mathrm{R}})\left[1 - \frac{1}{2}(1 - 8\beta)(M_{\mathrm{L}} - M_{\mathrm{R}}) + \mathrm{O}(M^3)\right] + M_p. \tag{46}$$

Here, the added pressure diffusion M_p is based on the previous expression, Eq. (21), but is made more general by inserting an extra scaling term M_*^{-m},

$$M_p = -\omega(\bar{M}) M_*^{-m} \frac{p_{\mathrm{R}} - p_{\mathrm{L}}}{\rho_{1/2} a_{1/2}^2}, \tag{47}$$

where $\omega(\bar{M}) = K_p \max(1 - \sigma \bar{M}^2) = \mathrm{O}(1)$.

If $\beta = 1/8$, then the interface velocity is simply evaluated by a simple average of M_{L} and M_{R} up to $\mathrm{O}(M_*^3)$, besides M_p. It is interesting to note that this choice of β was suggested previously under a very different criterion [16].

Using Eq. (45), the interface Mach number in Eq. (46) becomes, as $M_* \to 0$,

$$M_{1/2} = \frac{1}{2}(M_{\mathrm{L}} + M_{\mathrm{R}}) - \omega(\bar{M}) M_*^{-m} \frac{\bar{p}_{\mathrm{R}} - \bar{p}_{\mathrm{L}}}{\bar{p}_{1/2} a_{1/2}^2} = \frac{1}{2} M_*(\hat{M}_{\mathrm{L}} + \hat{M}_{\mathrm{R}}) - \omega(\bar{M}) M_*^{-m} \frac{p_{\mathrm{R}} - p_{\mathrm{L}}}{p_{1/2} a_{1/2}^2}. \tag{48}$$

For $m \geqslant 0$, the pressure diffusion is the leading term in $M_{1/2}$, hence the mass flux $\dot{m}_{1/2}$.

Similarly, we find the pressure flux for $|M| \leqslant 1$,

$$\bar{p}_{1/2} = \tfrac{1}{2}(\bar{p}_{\mathrm{L}} + \bar{p}_{\mathrm{R}}) - \tfrac{1}{2}[D_p(M_{\mathrm{R}})\bar{p}_{\mathrm{R}} - D_p(M_{\mathrm{L}})\bar{p}_{\mathrm{L}}] + \bar{p}_u, \tag{49}$$

where

$$D_p(M) = \frac{M}{2}[(3 + 4\alpha) - (1 + 8\alpha)M^2 + 4\alpha M^4]; \quad -3/4 \leqslant \alpha \leqslant 3/16. \tag{50}$$

Noticing that care is taken in this section to distinguish the dimensional quantities, denoted with an "overbar", from the non-dimensional ones. Generalizing Eq. (26) by introducing an unspecified function φ,

$$\bar{p}_u = -\varphi(M_{\mathrm{L}}, M_{\mathrm{R}})(\bar{\rho}_{\mathrm{L}} + \bar{\rho}_{\mathrm{R}}) \bar{a}_{1/2} M_*^n (\bar{u}_{\mathrm{R}} - \bar{u}_{\mathrm{L}}), \tag{51}$$

where the function $\varphi(M_{\mathrm{L}}, M_{\mathrm{R}})$ is to be determined later. Again the scaling term M_*^n has been inserted for this analysis to allow a proper scaling to be determined later. It is anticipated that $n > 0$ so that $\bar{p}_u$ remains bounded as $M_* \to 0$. In our previous studies, the parameter α has been set equal to a constant of 3/16. However, we also wish to have a possibility of having a more suitable value of α for the low speed regime. To achieve this, we define

$$\alpha = -\tfrac{3}{4} + \hat{\alpha}(M), \tag{52}$$

where we require that

$$\hat{\alpha} = \tfrac{15}{16} \quad \forall |M| \geqslant 1 \tag{53}$$

so that the value of 3/16 is returned for α. Observing Eqs. (50) and (52), one may require that $\hat{\alpha}$ be small when $M = \mathrm{O}(M_*) \ll 1$. Here, we consider the limiting case when $M \ll 1$ and write

$$\alpha = -\tfrac{3}{4} + M_*^l g(\hat{M}), \quad l > 0, \tag{54}$$

where $g(\hat{M}) = \mathrm{O}(1) > 0$ so that the monotonicity constraint (given in [16]) is met. Also, $l > 0$ is required such that α remains bounded as $M_* \to 0$. Substituting Eq. (54) into Eq. (50) gives the leading term of D_p,

$$D_p(M) = M_*^{l+1} \hat{D}_p(\hat{M}) + \mathrm{O}(M_*^3), \quad \hat{D}_p(\hat{M}) = \mathrm{O}(1). \tag{55}$$

Hence,

$$\bar{p}_{1/2} = \tfrac{1}{2}(\bar{p}_\mathrm{L} + \bar{p}_\mathrm{R}) + \bar{p}_u + \tfrac{1}{2} M_*^{l+1} [\hat{D}_p(\hat{M}_\mathrm{L}) \hat{M}_\mathrm{L} \bar{p}_\mathrm{L} - \hat{D}_p(\hat{M}_\mathrm{R}) \hat{M}_\mathrm{R} \bar{p}_\mathrm{R}] + \mathrm{O}(M_*^3). \tag{56}$$

After non-dimensionalization as described earlier $p = \bar{p}/\bar{\rho}_* \bar{a}_*^2$, the interface pressure becomes,

$$\begin{aligned} p_{1/2} = {} & \tfrac{1}{2}(p_\mathrm{L} + p_\mathrm{R}) - M_*^{n+1} \varphi(M_\mathrm{L}, M_\mathrm{R})(\rho_\mathrm{L} + \rho_\mathrm{R}) a_{1/2}(u_\mathrm{R} - u_\mathrm{L}) + \tfrac{1}{2} M_*^{l+1} [\hat{D}(\hat{M}_\mathrm{L}) \hat{M}_\mathrm{L} p_\mathrm{L} - \hat{D}(\hat{M}_\mathrm{R}) \hat{M}_\mathrm{R} p_\mathrm{R}] \\ & + \mathrm{O}(M_*^3), \quad l, n > 0. \end{aligned} \tag{57}$$

Finally, we are ready to evaluate the mass, momentum and energy fluxes at the interface 1/2 as follows. First, let

$$\hat{\dot{m}}_{1/2} = a_{1/2} \rho_{j/j+1} \left[\frac{1}{2}(\hat{M}_j + \hat{M}_{j+1}) - M_*^{-(1+m)} \hat{K}_{p_{1/2}} (p_{j+1} - p_j) \right], \tag{58}$$

where

$$\hat{K}_{p_{1/2}} = \omega(\bar{M}) / (\rho_{1/2} a_{1/2}^2), \tag{59}$$

and as in Eq. (9),

$$\rho_{j/j+1} = \begin{cases} \rho_j & \text{if } [\cdots] \text{ of Eq. (58)} > 0, \\ \rho_{j+1} & \text{otherwise.} \end{cases} \tag{60}$$

Then,

$$\bar{F}_{1/2}^{(1)} = (\bar{\rho}_* \bar{u}_*) f_{1/2}^{(1)} = (\bar{\rho}_* \bar{u}_*) \hat{\dot{m}}_{1/2}, \tag{61}$$

$$\bar{F}_{1/2}^{(2)} = (\bar{\rho}_* \bar{u}_*^2) f_{1/2}^{(2)} = (\bar{\rho}_* \bar{u}_*^2) \left[\hat{\dot{m}}_{1/2} u_{1/2} + \frac{p_{1/2}}{M_*^2} \right], \tag{62}$$

$$\bar{F}_{1/2}^{(3)} = (\bar{\rho}_* \bar{u}_* \bar{a}_*^2) f_{1/2}^{(3)} = (\bar{\rho}_* \bar{u}_* \bar{a}_*^2) \hat{\dot{m}}_{1/2} H_{1/2}. \tag{63}$$

Again, the quantities $(u_{1/2}, H_{1/2})$ are convected and are defined in the same fashion as $\rho_{1/2}$ in Eq. (60). It is noted that the factor M_*^2 in the pressure term is due to the fact that $p_{1/2}$ has been non-dimensionalized by $\bar{a}_*^2$.

Substitution of the above equations into the semi-discrete equations written in the finite-volume form,

$$\Delta x \frac{\mathrm{d}}{\mathrm{d}t} \mathbf{q} + \Delta \mathbf{f} = 0, \tag{64}$$

and using the series expansion given in Eq. (37), we obtain, after some lengthy algebraic manipulations, a system of semi-discrete equations that are valid for $M_* \to 0$ and specific for the numerical fluxes AUSM$^+$-up. The resulting equations are somewhat involved and we shall only give the following summary.

Let us now consider the case when $m = n = 1$.

A discrete version of the Laplacian equation for the pressure field holds for the zeroth and first-order solutions from the continuity equation. Combining both continuity and momentum equations yields, for arbitrary states of (ρ, u, e) and $M_* \to 0$,

$$\Delta p_j^{(l)} = p_{j+1}^{(l)} - p_j^{(l)} = 0, \quad l = 0, 1, \ \forall j. \tag{65}$$

This implies $p_j = p_{j-1} = p_{j+1}\ \forall j$ for the first two orders of the series in p. That is, the pressure is constant in space up to and including $O(M_*)$. Hence, we have the expansion of p in the discrete system,

$$p(\vec{x}, t) = p^{(0)}(t) + M_*^2 p^{(2)}(\vec{x}, t) + \cdots \tag{66}$$

This also implies that the solution is free of odd–even oscillations up to $O(M_*^2)$.

The energy equation does not yield any new information to alter the above result, as in the case of continuum system.

Hence, Eq. (66), resulting from our numerical scheme, is consistent with the theoretical result, Eq. (40) of the continuous system. The implication is that the current scheme will hold its accuracy consistently for computations of low Mach number flows because it does not introduce an error of $O(M_*)$. But this is not true for the original AUSM$^+$ scheme [16], as evident later in Fig. 24.

Interestingly, one can find that the discrete equations are the counterpart of the continuous equations, but with added diffusion terms.

Lemma. *The discrete system derived above for $M_* \to 0$ is a consistent, to the order of Δx, and dissipative approximation to the continuum system, i.e.,*

$$\frac{\partial \rho^{(0)}}{\partial t} + \nabla \cdot \rho^{(0)} \vec{u}^{(0)} = \frac{\partial}{\partial x_k}\left(\mu \frac{\partial p^{(2)}}{\partial x_k}\right), \tag{67}$$

where the dissipation coefficient

$$\mu = O(\Delta x) > 0, \tag{68}$$

and is independent of M_*. The dissipation is directly related to the spatial variation of the second-order pressure expansion $p^{(2)}$. The proof is given in Appendix A.

Since $n = 1$, the combination of M_*^n in $p_{1/2}$ and the speed of sound is effectively equivalent to the use of numerical speed of sound, but only used in the velocity diffusion term $p_{1/2}$ and nowhere else. It also reveals that the concept of numerical sound suggested in [8] is sound, but how and where it should be applied was done heuristically, short of a formal derivation.

Now we are reminded that the above derivation is valid for $M_* \to 0$ and the basic scheme given in Section 2 should return when $M_* = O(1)$. The insertion of terms like M_*^{-m} and M_*^{-n} in M_p and p_u is only required as $M_* \to 0$ and these terms should become exactly unity as $M_* = O(1)$. Since the scaling function f_a as given in Eq. (14) conveniently fulfills this requirement, we shall use f_a to take place of M_* in M_p, p_u and α so that the new AUSM$^+$-up becomes valid for all speeds.

3.3. Algorithm: AUSM$^+$-up for all speeds

The final algorithm is given as follows. First, one defines,

$$M_{L/R} = \frac{u_{L/R}}{a_{1/2}}, \tag{69}$$

where $a_{1/2}$ is defined either by Eq. (30) or a simple average of a_L and a_R. For multi-dimensional flows, $u = V \cdot \mathbf{n}$, with $\mathbf{n}$ being the unit normal vector of the cell face under consideration.

$$\bar{M}^2 = \frac{(u_L^2 + u_R^2)}{2a_{1/2}^2}, \tag{70}$$

$$M_o^2 = \min(1, \max(\bar{M}^2, M_\infty^2)) \in [0, 1], \tag{71}$$

$$f_a(M_o) = M_o(2 - M_o) \in [0, 1], \tag{72}$$

$$M_{1/2} = \mathscr{M}_{(4)}^+(M_L) + \mathscr{M}_{(4)}^-(M_R) - \frac{K_p}{f_a}\max(1 - \sigma\bar{M}^2, 0)\frac{p_R - p_L}{\rho_{1/2} a_{1/2}^2}, \quad \rho_{1/2} = (\rho_L + \rho_R)/2, \tag{73}$$

where $0 \leqslant K_p \leqslant 1$ and $\sigma \leqslant 1$.

Then, the mass and pressure fluxes are readily defined

$$\dot{m}_{1/2} = a_{1/2} M_{1/2} \begin{cases} \rho_{\mathrm{L}} & \text{if } M_{1/2} > 0, \\ \rho_{\mathrm{R}} & \text{otherwise} \end{cases} \tag{74}$$

and

$$p_{1/2} = \mathscr{P}^{+}_{(5)}(M_{\mathrm{L}}) p_{\mathrm{L}} + \mathscr{P}^{-}_{(5)}(M_{\mathrm{R}}) p_{\mathrm{R}} - K_u \mathscr{P}^{+}_{(5)} \mathscr{P}^{-}_{(5)} (\rho_{\mathrm{L}} + \rho_{\mathrm{R}})(f_a a_{1/2})(u_{\mathrm{R}} - u_{\mathrm{L}}) \tag{75}$$

using the parameters

$$\begin{aligned} \alpha &= \frac{3}{16}(-4 + 5 f_a^2) \in \left[-\frac{3}{4}, \frac{3}{16} \right], \\ \beta &= \frac{1}{8}, \end{aligned} \tag{76}$$

with $0 \leqslant K_u \leqslant 1$.

Finally, the whole flux is

$$\mathbf{f}_{1/2} = \dot{m}_{1/2} \begin{cases} \vec{\psi}_{\mathrm{L}} & \text{if } \dot{m}_{1/2} > 0, \\ \vec{\psi}_{\mathrm{R}} & \text{otherwise,} \end{cases} + \mathbf{p}_{1/2}. \tag{77}$$

It is reminded that only in the pressure flux is the numerical speed of sound used, which is scaled by the factor f_a, but nowhere else.

This scheme is still designated as AUSM^{+}-up since it incorporates both the velocity and pressure terms into AUSM^{+} scheme and the basic scheme is only a special version obtained by simply setting $f_a = 1$.

As noted previously, the basic scheme should be invoked when we consider the shock-tube type of problems in which the leading pressure term is not spatially uniform, even though the fluid velocity may be small, see the examples presented above.

In all calculations, we set $K_p = 0.25$, $K_u = 0.75$ and $\sigma = 1.0$ (except in Fig. 9 shown before).

4. Results

In this section, we shall present numerical results to address the issues on robustness and accuracy for a variety of 2D and 3D flow problems and flow speed regimes, on a variety of grid topologies, including the chimera grid. Also, to verify that the proposed scheme holds when it is combined with various time-integration methods and codes, we employed four different CFD codes, including the OVERFLOW [28] and Swift [29] codes, with six different integration schemes, such as implicit ADI, implicit LU, explicit 4-stage Runge–Kutta with residual smoothing, and explicit 2-stage Runge–Kutta schemes. The implicit ADI and explicit 4-stage schemes have an option of turning on the local preconditioner of Weiss–Smith [3].

For all viscous calculations, the flow is assumed to be fully turbulent. The turbulence models used in this study include several popular ones such as Spalart–Allmaras's (S–A) [32], Mentor's k–ϵ (SST) [30], and Wilcox's k–ω [31] models.

The calculations were carried out using the same set of parameters associated with the above-mentioned time marching procedures, while no attempts were made to find an optimal set of parameters. Most of the 2D and 3D cases were solved with the OVERFLOW code and the turbomachinery problem was computed using the Swift code. To extend the spatial accuracy from that of first order and maintain monotonicity, we used the standard limiter, see [33].

A useful indicator adopted in this study for measuring the robustness of the scheme is the convergence rate. That is, a robust scheme should maintain the same convergence rate, irrespective of Mach numbers or other flow conditions, and should remain stable with different time integration schemes.

4.1. 2D cylinder

First, we show in Fig. 18 the pressure contours of a third-order accurate solution over a blunt body with $M_\infty = 10$. Not only is the solution free of carbuncle phenomena, but also the pressure contours are smooth,

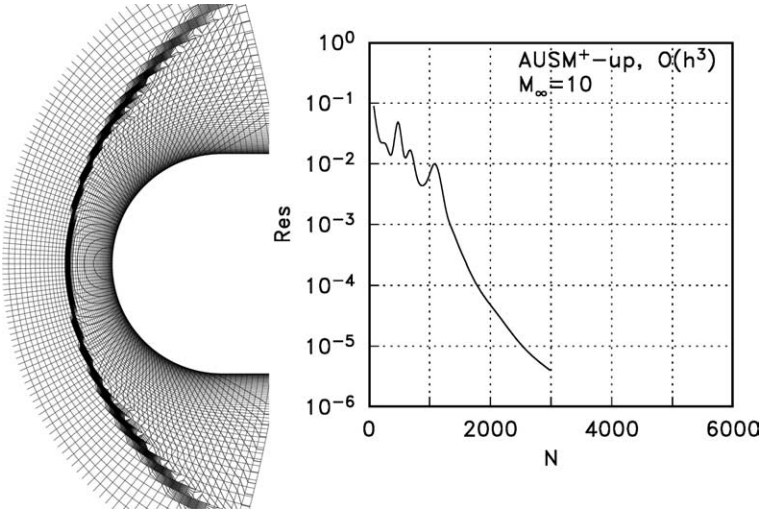

Fig. 18. Blunt body problem, $M_\infty = 10$.

specifically near the stagnation point and sonic line regions. The convergence history also exhibits a continuous drop in residual.

4.2. Shuttle external tank

This is an axisymmetric Shuttle External Tank geometry with a sharp nose, a blunt base and a tiny notch at the mid-length. There is a significant zone of flow separation in the base. The grid number is 88×60. The free stream Reynolds number is 10,000 and the boundary layer is assumed tripped at the leading edge. Hence, the flow is treated as fully turbulent and described by the S–A model. We have tested conditions from low Mach number, transonic, to supersonic speeds. This case was used previously [8,9] to study the effectiveness of numerical speed of sound and preconditioning matrix. We again used this case to test the new scheme for its performance in terms of accuracy and convergence. In all calculations of this problem, we made 200 steps for each of two coarser grids prior to the finest grid, on which 3000 more steps were continued unless noted otherwise.

Displayed in Fig. 19 are the convergence histories of two schemes for various Mach numbers: (1) AUSM$^+$ [16] and (2) AUSM$^+$-up. The Weiss–Smith preconditioner was used in both cases. The residuals of the first scheme for the low Mach-number solutions stall after a drop of three to four orders of magnitude. These drops, although not especially admirable, would have been acceptable in many situations. However, a close

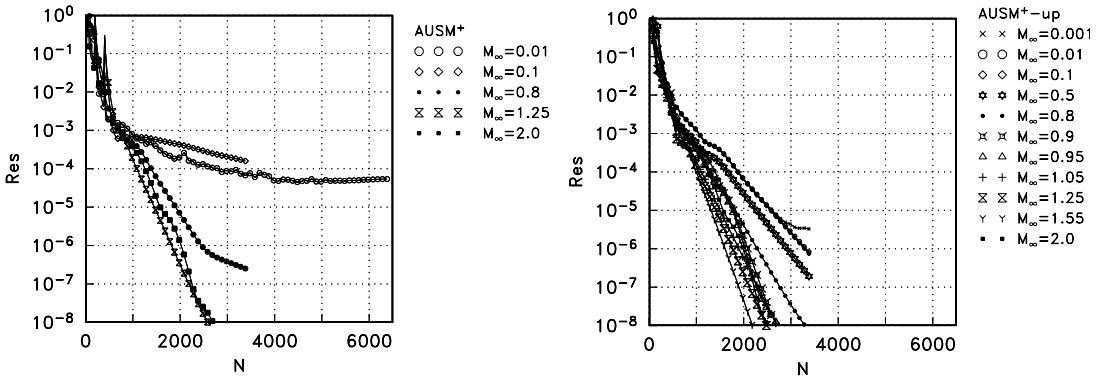

Fig. 19. Comparison of convergence rates between AUSM$^+$ and AUSM$^+$-up. Left: AUSM$^+$; Right: AUSM$^+$-up.

examination of the solution reveals that it is completely unacceptable even after additional 3000 steps, as shown in Fig. 20. It appears that there is a false boundary (exactly aligned with a grid line) at which information is unable to pass through. Hence, here is an example showing that one should be cautious about assessing the convergence of solution when reading only the residual history in the case of low Mach-number solutions. Furthermore, we show in Fig. 20 the AUSM$^+$-up solution at $N = 1600$ steps at which the residual has been dropped to the level approximately equal to that of AUSM$^+$, at $N = 6400$. The solution now is well behaved and is as good as the final solution at $N = 3400$ (hence, not included), at which the residual has been further reduced by two orders.

A further examination of convergence histories reveals some interesting characteristics of the new scheme, as displayed in Fig. 21.

(1) A monotonic convergence is observed for all Mach numbers.
(2) A Mach-number independent convergence rate is observed in the low Mach number regime, with a nearly identical rate for $M_\infty \leqslant 0.5$. It may be noted that the stall in residual in the $M_\infty = 0.001$ case towards the end is due to the fact that the absolute residual for this very low Mach number has already reached the machine truncation error. (A better way of handling the low Mach number calculations might be by subtracting the free stream pressure in the code.)
(3) Similarly, the convergence for transonic cases is also essentially Mach number independent.

In the previous study [9], it was found that a preconditioning matrix must be used in order to get a stable solution for $M_\infty \leqslant 0.1$. It was discovered in this study that the current scheme AUSM$^+$-up actually remained

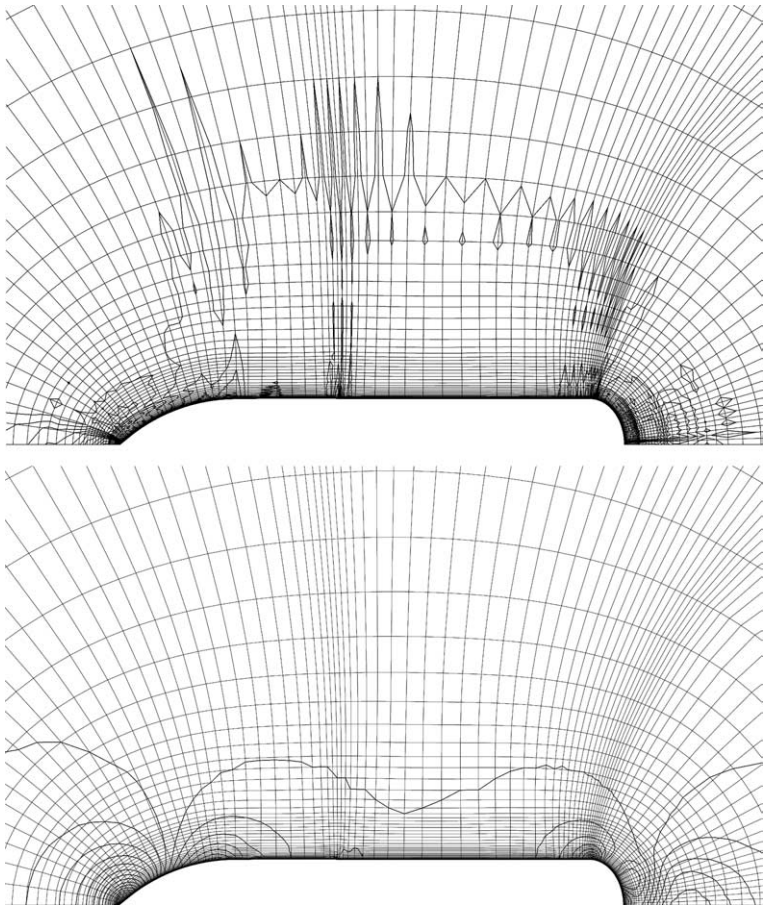

Fig. 20. Pressure contours for the shuttle external tank problem for $M_\infty = 0.01$. Top: AUSM$^+$; Bottom: AUSM$^+$-up.

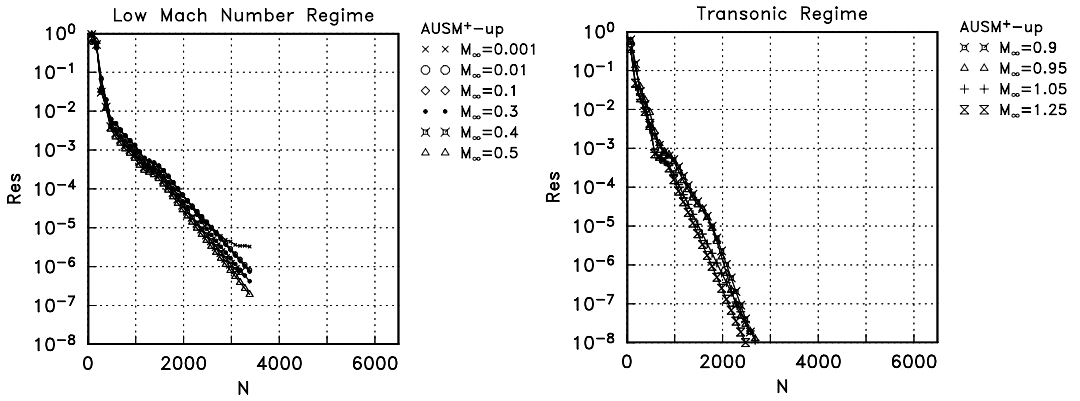

Fig. 21. Convergence history by AUSM$^+$-up.

stable without using the preconditioning matrix, although the convergence stalled after having dropped by at least four orders as displayed in Fig. 22, similar to what appears in Fig. 19 with the AUSM$^+$. However, the solution is completely different from that of AUSM$^+$, and in fact gives a correct behavior and smooth contours, completely due to proper rescaling of the flux formula for low speeds. Furthermore, the pressure coefficients on the surface of the tank at $M_\infty = 0.01$ by both the preconditioned and non-preconditioned time integration schemes are compared in Fig. 23; both results are essentially identical. This finding is important in the sense that reliable solutions can be obtained even without resorting to a local preconditioner. Hence, the current scheme is a reliable one, not only for calculating low Mach number flows but also throughout the entire speed regimes.

To summarize the validity of the present scheme, we show in Fig. 24 the pressure differences in the flowfields with respect to the free-stream Mach number. Recall that differences in pressure among various spatial locations, according to the asymptotic analysis, should be proportional to M_∞^2 only. The agreement of the numerical results with that of asymptotic analysis is astonishing; the scheme accurately predicts that the pressure variations (in space) are proportional to the M_∞^2. This trend continues up to $M_\infty = 1$ before a shock forms in the flowfield, even though the asymptotic analysis is meant to be valid only for low Mach number. It is reminded that the computations were carried out with the Navier–Stokes equations. This implies that the viscous terms play little role in altering the pressure variations established by the Euler equations, also confirmed by the asymptotic analysis so long as $M_* \gg 1/Re$. This condition is met for all the cases considered, including the case of the smallest Mach number $M_* = \mathrm{O}(10^{-3})$.

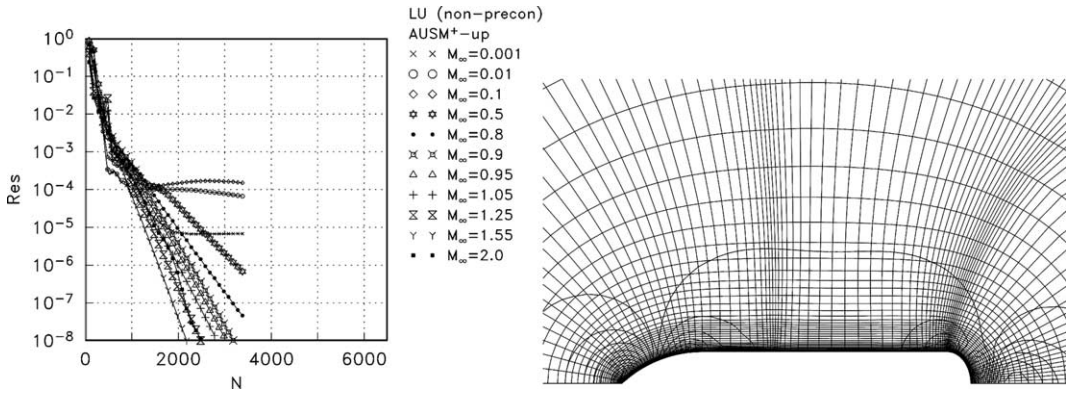

Fig. 22. Convergence histories of various M_∞ using a non-preconditioned LU integration scheme and AUSM$^+$-up and pressure contours for $M_\infty = 0.01$.

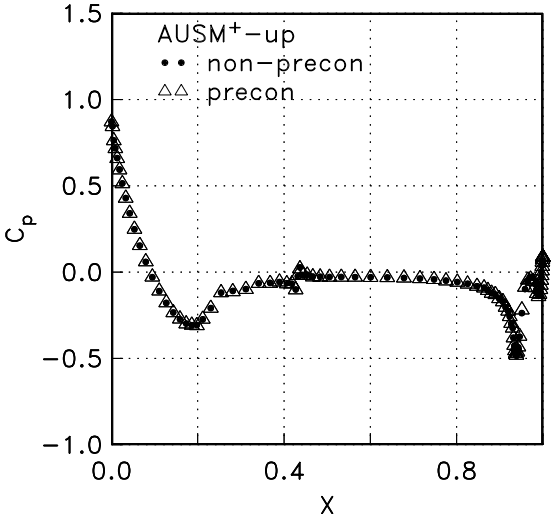

Fig. 23. Comparison of pressure distributions of AUSM$^+$-up between using non-preconditioned LU and preconditioned integration schemes.

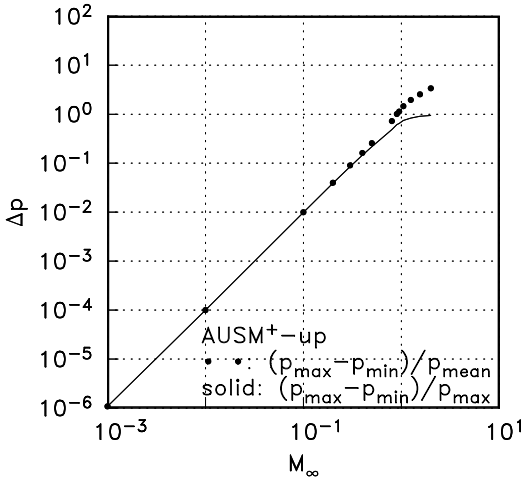

Fig. 24. Pressure variations vs. M_∞ demonstrating the correct scaling of pressure variations in space begins only in the O(M^2) series expansion.

It is noted that viscous grid effect can be taken into account in the preconditioning matrix in terms of the Reynolds number based on the streamwise grid spacing Δx, denoted as $Re_{\Delta x}$. A simple and robust procedure for including the effect of viscosity and grid aspect ratio effects has been suggested in [35]. This viscous scaling becomes dominant when $M \ll 1/Re_{\Delta x}$. In the present calculations, no such viscous scaling was employed in the preconditioning matrix. However, the convergence histories, particularly those for both $M_\infty = 10^{-2}$ and 10^{-3}, do not appear deteriorated.

4.3. Axisymmetric bump

Transonic flows over an axisymmetric bump (or dubbed as Bachalo–Johnson bump) was simulated for $Re_\infty = 2.66 \times 10^6$, $M_\infty = 0.875$ and 0.925 on an 181×101 grid. Experiments for this flow model were conducted to provide validation data for turbulence models development in a flowfield free from tunnel wall interference, three-dimensional effects and excessive unsteadiness [34]. Calculations with various turbulence models

were obtained; we shall only present in this paper the results from the two-equation SST model. Fig. 25 shows that the rate of convergence again is quite insensitive to the Mach number in spite of a considerable size of separated region, which results in a strongly curved shock at the foot. Fig. 26 shows that the calculated surface pressure distributions and shock locations agree very well with the measured data at both flow conditions.

4.4. Annular turbine vane

Numerical solution was carried out to compare with the data from an annular turbine vane experiment by Goldman and McLallin [36], on a $97 \times 37 \times 32$ grid, around the blade, blade-to-blade and spanwise, respectively. The Swift code [29] was used with a 4-stage Runge–Kutta scheme accelerated with a residual smoothing technique. The k–ω model was applied. Fig. 27 shows the comparison of the spanwise distribution of flow angles downstream of the vane. The AUSM$^+$-up scheme gives an excellent agreement with the data, while the centered scheme (JST) [38] yields a rather flat distribution and misses the peaks, indicating an excessive dissipation. Fig. 28 displays smooth pressure contours around the blade. Additional results and discussion for turbomachinery applications can be found in [6].

4.5. Wingbody

Turbulent flows using the S–A model over a wing-body configuration were calculated. The flow conditions are: $M_\infty = 0.8$, $Re_\infty = 0.166 \times 10^6$ and angle of attack of two degrees. Fig. 29 shows the geometry together

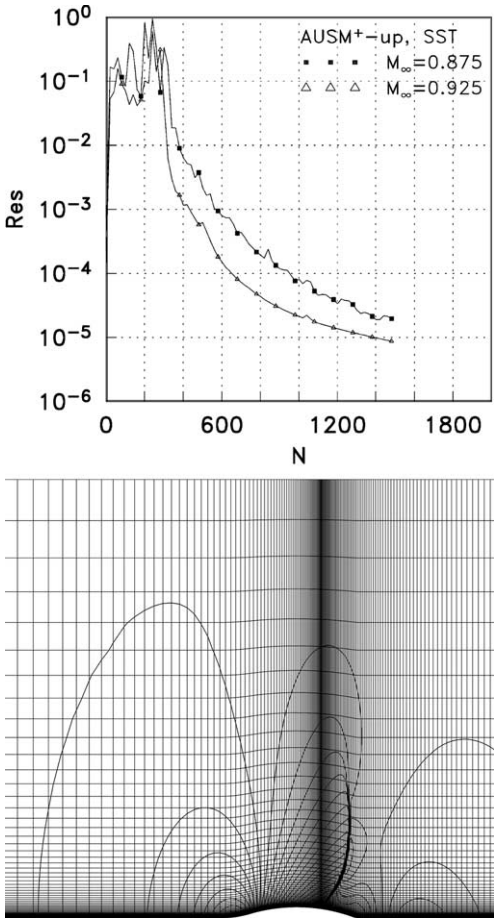

Fig. 25. Axisymmetric bump using SST model at $Re_\infty = 2.66 \times 10^6$ and $M_\infty = 0.875$ and 0.925. Top: convergence history; Bottom: pressure contours for the $M_\infty = 0.925$ flow.

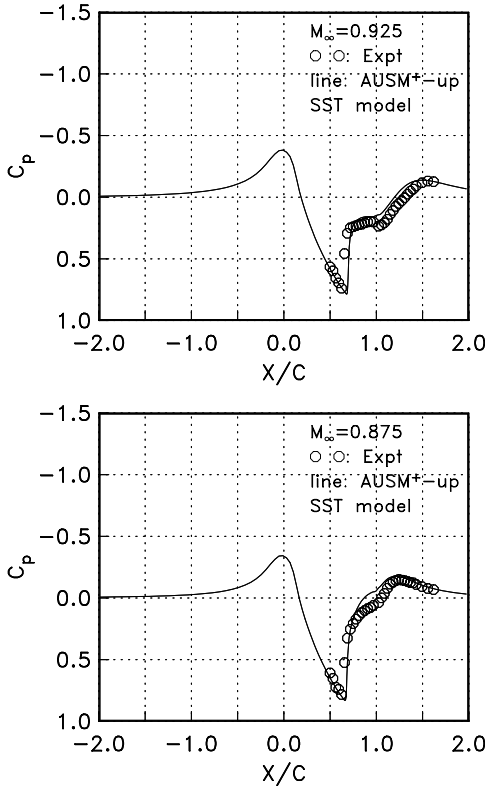

Fig. 26. Pressure distribution for an axisymmetric bump using SST model at $Re_\infty = 2.66 \times 10^6$ and $M_\infty = 0.925$ and 0.875.

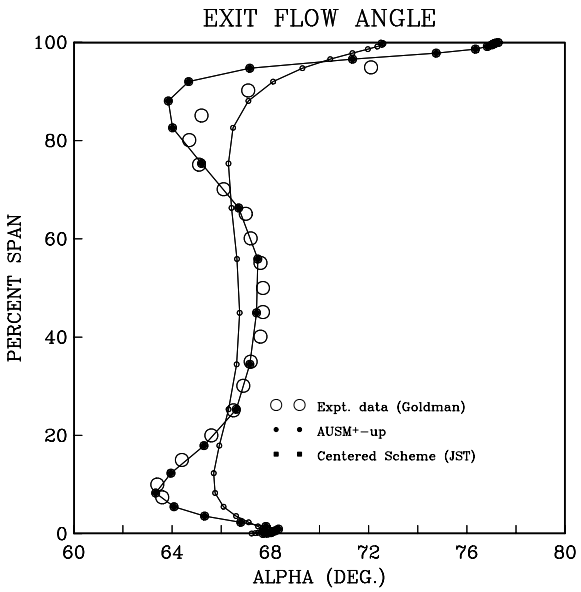

Fig. 27. Comparison of flow angles by AUSM$^+$-up and centered (JST) schemes for annular turbine vane.

with the sting, and the chimera (overset) grid which consists of seven subgrids, totaling 1.1 million grid points. Fig. 30 presents the pressure coefficients at various spanwise locations predicted by the AUSM$^+$-up, showing excellent agreement with the measured data [39]. Moreover, the pressure coefficients along the body, shown in

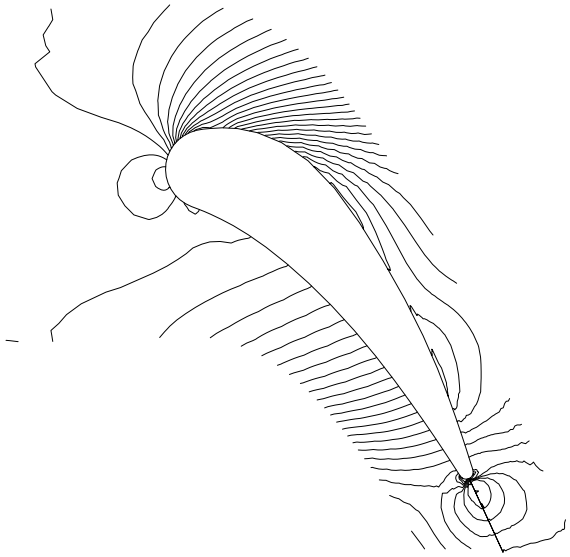

Fig. 28. Pressure contours for annular turbine vane.

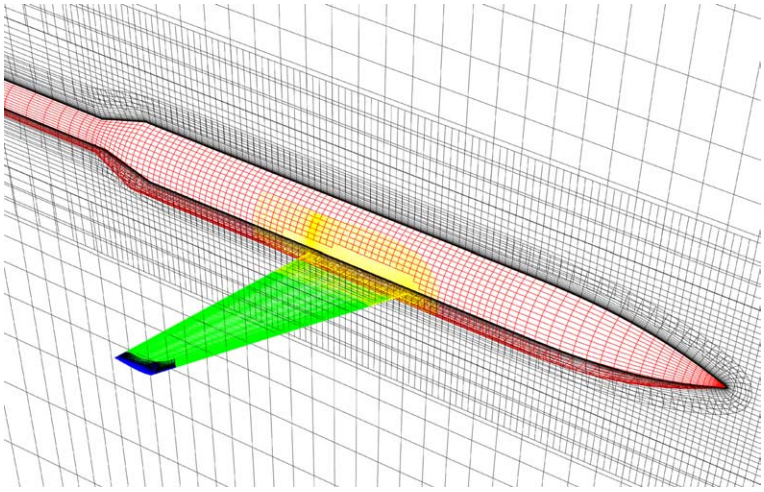

Fig. 29. Chimera grids used for solution of flow over a wingbody configuration.

Fig. 31, again exhibits excellent agreement with the data, even in the wing root region where a sharp geometrical variation is encountered.

Also, Fig. 32 displays a well-behaved convergence history, reducing the residual error by more than five orders of magnitude in 800 steps. The convergence of AUSM$^+$-up appears to be slightly improved over that of AUSM$^+$, also in the transonic regime.

4.6. High-lift trap-wing

Finally, we considered a 3D low speed flow over a high-lift three-element trap-wing configuration with wind-tunnel effects [37]. The flow conditions are: $M_\infty = 0.1498$, $Re_\infty = 14.7 \times 10^6$ and angle of attack of 20°. The geometry consists of a body pod, a wing, a full-span slat, a full-span flap and the tunnel walls, as displayed in Fig. 33. Rogers et al. [40] have performed an extensive numerical study of the aerodynamic characteristics of this configuration using the preconditioned version of the Roe scheme in the OVERFLOW code,

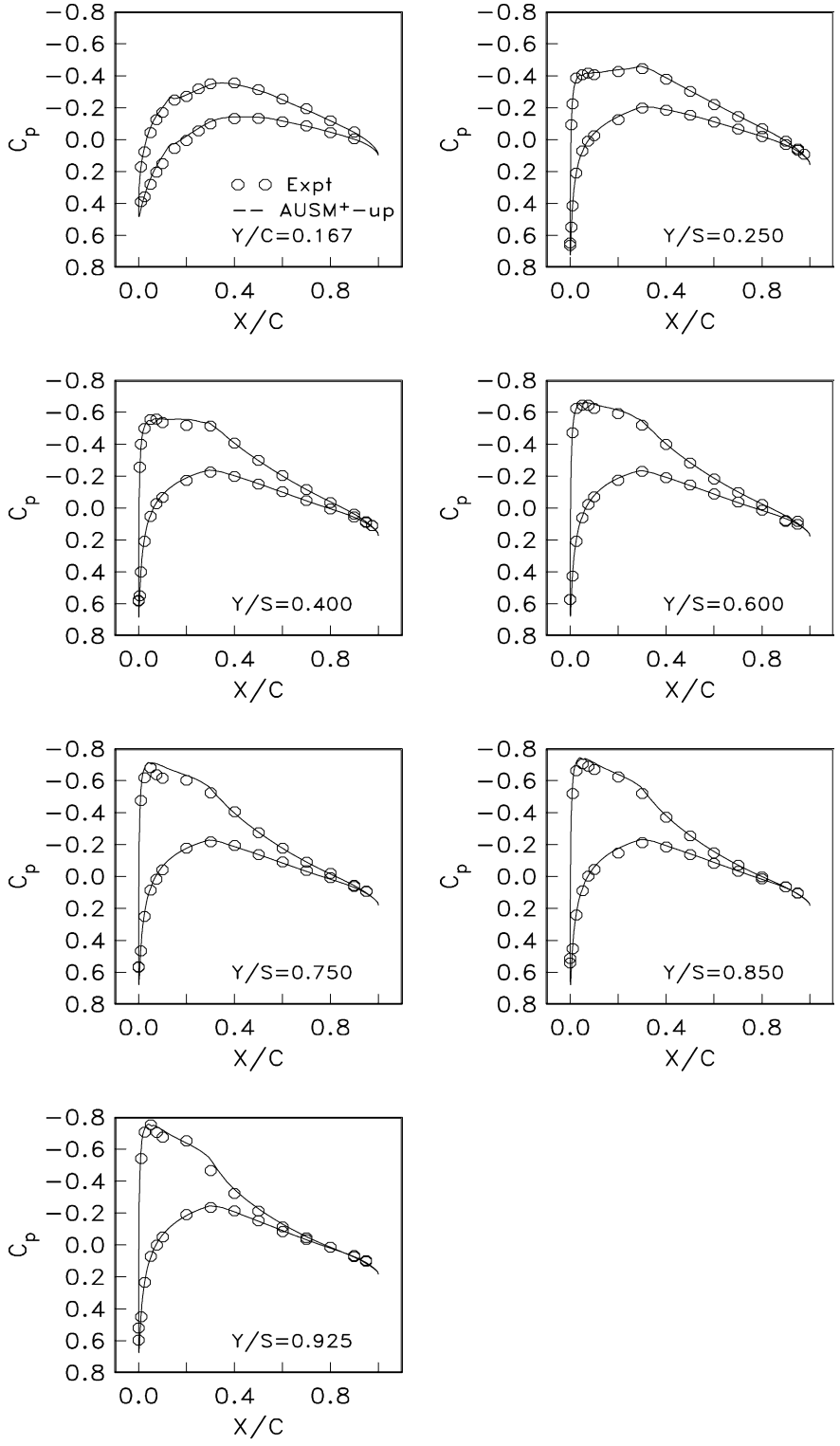

Fig. 30. Pressure distribution on the wing of a wingbody configuration using S–A model at $M_\infty = 0.8$, $\alpha = 2^\circ$, and $Re_\infty = 0.166 \times 10^6$.

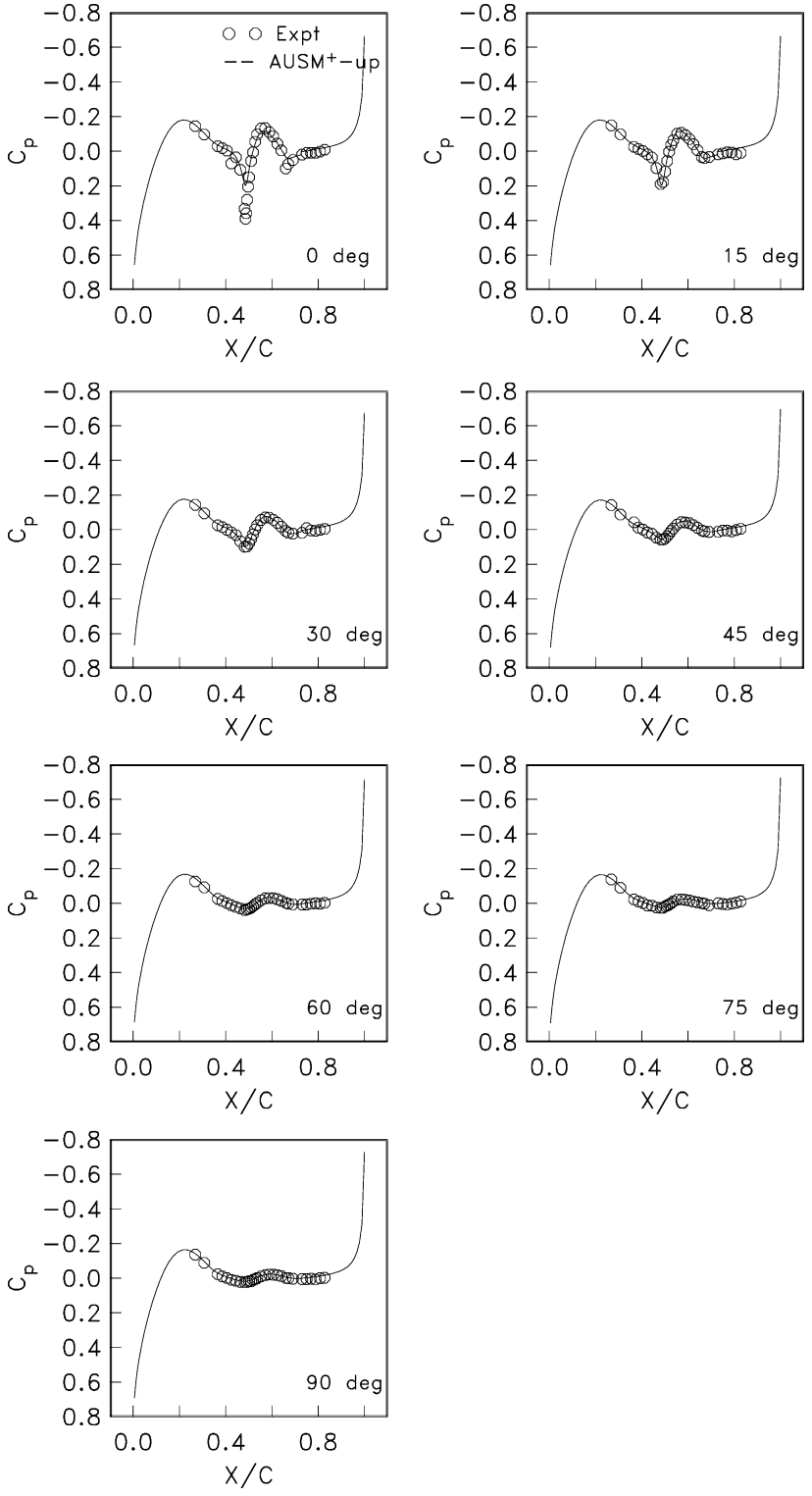

Fig. 31. Pressure distribution on the body of a wingbody configuration using S–A model at $M_\infty = 0.8$, $\alpha = 2°$, and $Re_\infty = 0.166 \times 10^6$.

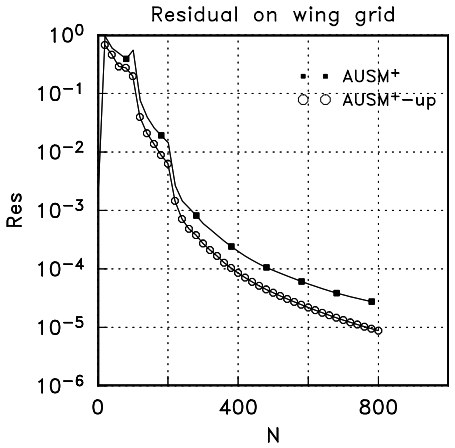

Fig. 32. Convergence history for a wingbody configuration using S–A model at $M_\infty = 0.8$, $\alpha = 2°$, and $Re_\infty = 0.166 \times 10^6$.

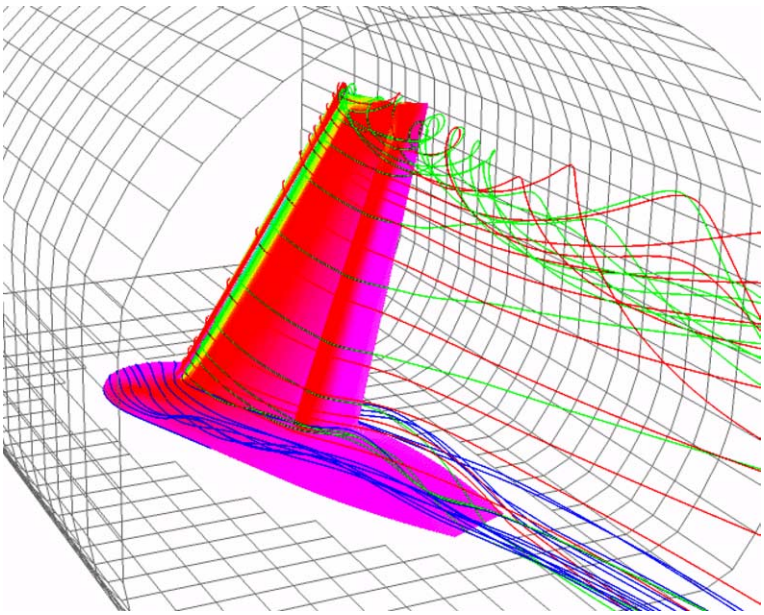

Fig. 33. Trap wing model in a wind tunnel, the tunnel grid is plotted every fourth grid point.

using the S–A one-equation model. In the present study, we used the AUSM$^+$-up instead. The chimera grid was composed of 14 subgrids with a total of 8.7 million grid points. The pressure distributions by the AUSM$^+$-up are seen in Fig. 34 in excellent agreement with the experimental data at various spanwise locations.

This case, along with others shown above, at least confirms that despite the multitude of complexities that may result from grid and turbulence modeling issues, a reliable numerical flux scheme can contribute to a reliable prediction of complex 3D flowfields.

5. Concluding remarks

A new version of the AUSM-family schemes, based on the low Mach number asymptotic analysis, has been described in this paper. The resulting scheme, called AUSM$^+$-up, has been demonstrated to be a reliable and effective one, not only for low Mach number, but also over the entire speed regimes, for a wide variety of flow problems over different geometries and grids. The solutions converge in a Mach-number-independent fashion and are accurate, in excellent agreement with corresponding measurements or analytical results.

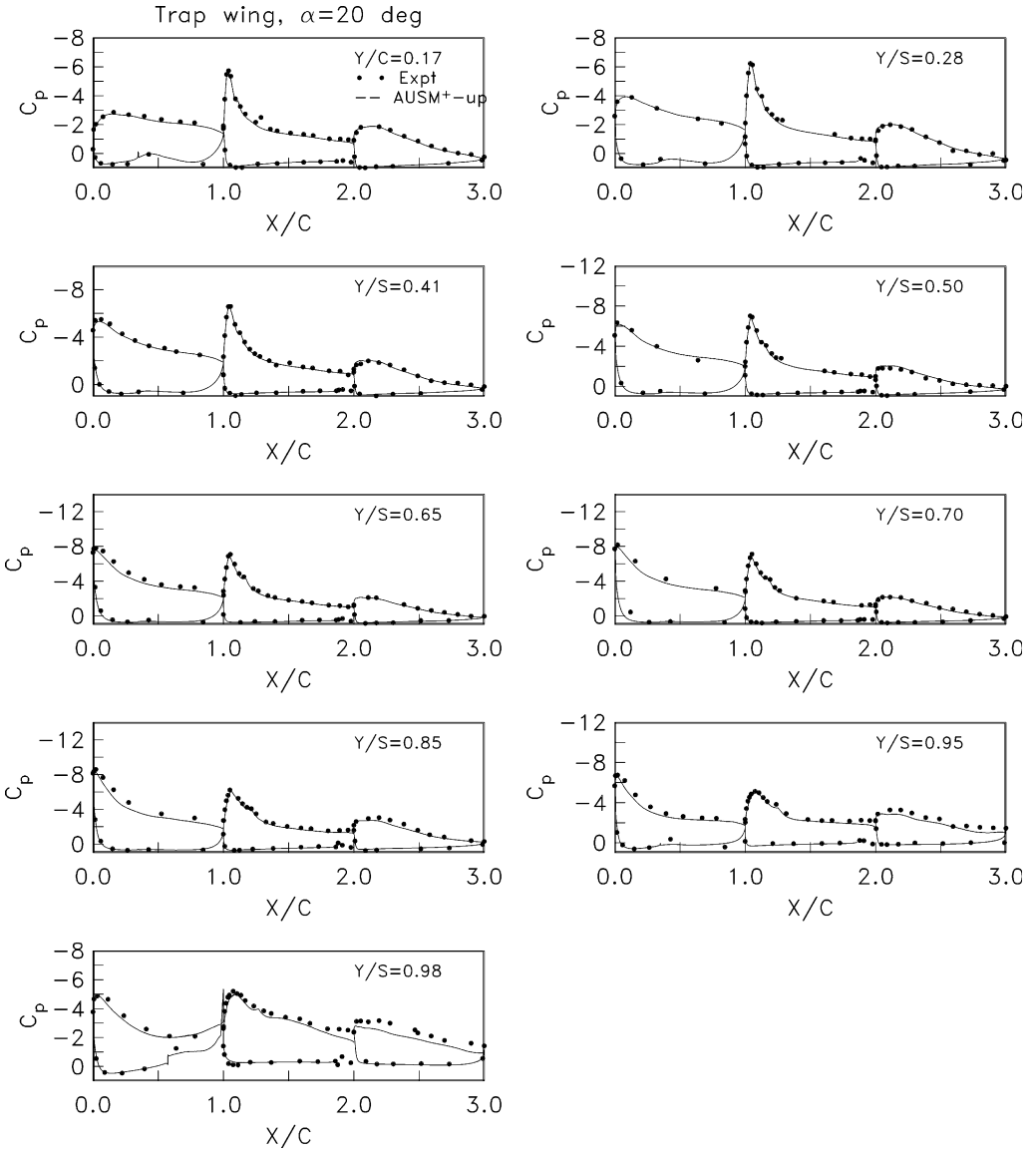

Fig. 34. Pressure distributions on three wing elements at various spanwise locations.

In addition, we showed that the AUSM$^+$-up possesses the following attributes: (1) exact capturing of a contact discontinuity, (2) exact capturing of a normal shock discontinuity with an entropy-satisfying property, (3) positivity preserving property, (4) solution free of carbuncle phenomenon (5) accurate solution of slowly moving contact and shock discontinuities, and (6) smooth transition through the sonic point.

Acknowledgments

The author acknowledges the generosity of Drs. Pieter Buning of NASA Langley and Rod Chima of NASA Glenn for providing the OVERFLOW and Swift codes and assistance in using the codes. This research, managed by Dr. Eric McFarland, was conducted under the support of Revolutionary Aeropropulsion Concept project of NASA Glenn Research Center. The author is grateful to the reviewers for their suggestions that have contributed the improvement of the paper. The discussion on σ^* in Eq. (32) is suggested by a reviewer.

Appendix A

In this appendix, we provide an expanded derivation for the lemma given in Section 3.2.

For the case of $m = n = 1$, we list the equations useful for the derivation

$$\hat{\dot{m}}_{1/2} = a_{1/2}\rho_{j/j+1}\left[\frac{1}{2}(\hat{M}_j + \hat{M}_{j+1}) - M_*^{-2}\hat{K}_{p_{1/2}}(p_{j+1} - p_j)\right], \tag{A.1}$$

where the leading term is associated with the pressure diffusion as $M_* \to 0$. The coefficient $\hat{K}_{p_{1/2}}$ can be further expanded as

$$\hat{K}_{p_{1/2}} = K_p/(\rho_{1/2}a_{1/2}^2) = \hat{K}^{(0)}_{p_{1/2}} + M_*\hat{K}^{(1)}_{p_{1/2}} + \mathrm{O}(M_*^2). \tag{A.2}$$

Consequently, the mass flux $\hat{\dot{m}}_{1/2}$ has the leading term

$$\hat{\dot{m}}_{1/2} = \frac{1}{M_*^2}a^{(0)}_{1/2}\rho^{(0)}_{j/j+1}\hat{K}^{(0)}_{p_{1/2}}\Delta_{1/2}p + \mathrm{O}\left(\frac{1}{M_*}\right) = \frac{1}{M_*^2}\hat{\dot{m}}^{(0)}_{1/2} + \mathrm{O}\left(\frac{1}{M_*}\right), \tag{A.3}$$

where we let $\Delta_{1/2}p = p_{j+1} - p_j$ and similarly $\Delta_{-1/2}p = p_j - p_{j-1}$.

Furthermore, the leading fluxes become

$$\bar{F}^{(1)}_{1/2} = (\bar{\rho}_*\bar{u}_*)f^{(1)}_{1/2} = \frac{1}{M_*^2}(\bar{\rho}_*\bar{u}_*)\hat{\dot{m}}^{(0)}_{1/2} + \cdots, \tag{A.4}$$

$$\bar{F}^{(2)}_{1/2} = (\bar{\rho}_*\bar{u}_*^2)f^{(2)}_{1/2} = \frac{1}{M_*^2}(\bar{\rho}_*\bar{u}_*^2)\left[\hat{\dot{m}}^{(0)}_{1/2}u_{1/2} + \frac{1}{2}(p_{j+1} + p_j)\right] + \cdots, \tag{A.5}$$

$$\bar{F}^{(3)}_{1/2} = (\bar{\rho}_*\bar{u}_*\bar{a}_*^2)f^{(3)}_{1/2} = \frac{1}{M_*^2}(\bar{\rho}_*\bar{u}_*\bar{a}_*^2)\hat{\dot{m}}^{(0)}_{1/2}H^{(0)}_{1/2} + \cdots \tag{A.6}$$

Notice that the quantities $(\rho_{j/j+1}, u_{1/2}, H_{1/2}, a_{1/2})$ are defined in the same manner as before.

Substitution of the above equations into the semi-discrete equations,

$$\Delta x\frac{\mathrm{d}}{\mathrm{d}t}\mathbf{q} + \mathbf{f}_{1/2} - \mathbf{f}_{-1/2} = 0 \tag{A.7}$$

yields that the time-dependent terms are of higher order and the leading terms of $\mathrm{O}(1/M_*^2)$ are the spatial difference terms, as in the continuum case. That is, the continuity and momentum equations produce

$$a^{(0)}_{1/2}\rho^{(0)}_{j/j+1}\hat{K}^{(0)}_{p_{1/2}}\Delta_{1/2}p - a^{(0)}_{-1/2}\rho^{(0)}_{j-1/j}\hat{K}^{(0)}_{p_{-1/2}}\Delta_{-1/2}p = 0 \tag{A.8}$$

and

$$a^{(0)}_{1/2}\rho^{(0)}_{j/j+1}u^{(0)}_{1/2}\hat{K}^{(0)}_{p_{1/2}}\Delta_{1/2}p - a^{(0)}_{-1/2}\rho^{(0)}_{j-1/j}u^{(0)}_{-1/2}\hat{K}^{(0)}_{p_{-1/2}}\Delta_{-1/2}p + \tfrac{1}{2}(\Delta_{1/2}p + \Delta_{-1/2}p) = 0. \tag{A.9}$$

Combining both equations gives, for an arbitrary velocity field $u_{\pm 1/2}$,

$$\Delta_{1/2}p^{(0)} = p^{(0)}_{j+1} - p^{(0)}_j = 0 \tag{A.10}$$

and

$$\Delta_{-1/2}p^{(0)} = p^{(0)}_j - p^{(0)}_{j-1} = 0 \quad \forall j. \tag{A.11}$$

Hence, we get

$$p^{(0)}_j(t), \quad \forall j, \quad \Longleftrightarrow \quad p^{(0)}_j = \text{constant in space}. \tag{A.12}$$

This exactly reproduces the result of the continuum system for $M_* \to 0$. It can be shown in the same algebraic procedure that

$$\Delta_{\pm 1/2}p^{(1)} = 0 \quad \text{and} \quad p^{(1)}_j(t). \tag{A.13}$$

It is anticipated that the next expansion of series will involve the zeroth-order convection velocity $u^{(0)}$ simultaneously with the second-order pressure $p^{(2)}$ in the mass flux $\hat{m}_{\pm 1/2}$. After some straightforward but somewhat lengthy algebraic manipulations, we get

$$\Delta x \frac{\partial \rho_j^{(0)}}{\partial t} + \rho_{j/j+1}^{(0)} \left[\frac{1}{2}(u_j^{(0)} + u_{j+1}^{(0)}) - a_{1/2}^{(0)} \hat{K}_{p_{1/2}}^{(0)} \Delta_{1/2} p^{(2)} \right] - \rho_{j-1/j}^{(0)} \left[\frac{1}{2}(u_j^{(0)} + u_{j-1}^{(0)}) - a_{-1/2}^{(0)} \hat{K}_{p_{-1/2}}^{(0)} \Delta_{-1/2} p^{(2)} \right] = 0. \tag{A.14}$$

The spatial difference term can be considered as a second-order accurate discrete approximation to the derivative by taking $\Delta x \to 0$. Hence,

$$\frac{\partial \rho^{(0)}}{\partial t} + \frac{\partial}{\partial x} \rho^{(0)} u^{(0)} = \frac{\partial}{\partial x} \left(\mu \frac{\partial p^{(2)}}{\partial x} \right) + \mathrm{O}(\Delta x^2), \tag{A.15}$$

with

$$\mu = \rho^{(0)} a^{(0)} \hat{K}_p^{(0)} \Delta x > 0, \tag{A.16}$$

where the coefficient is positive definite. Hence, the discrete system is a dissipative one. The coefficient is a function of the zeroth-order thermodynamics variables only and is independent of characteristic Mach number M_*.

The above has completed the proof of the lemma.

References

[1] E. Turkel, Preconditioned methods for solving incompressible and low speed compressible equations, Journal of Computational Physics 72 (1987) 277–298.

[2] Y.H. Choi, C.L. Merkle, The application of preconditioning in viscous flows, Journal of Computational Physics 105 (1993) 207–223.

[3] J.M. Weiss, W.A. Smith, Preconditioning applied to variable and constant density time-accurate flows on unstructured meshes, AIAA Paper 94-2209, June 1994.

[4] B. van Leer, W.T. Lee, P.L. Roe, Characteristic time stepping or local preconditioning of the Euler equations, in: 10th AIAA CFD Conference, Paper 91-1552-CP, 1991.

[5] P.L. Roe, Approximate Riemann solvers, parameter vectors, and difference schemes, Journal of Computational Physics 43 (1981) 357–372.

[6] R.C. Chima, M.-S. Liou, Comparison of the AUSM$^+$ and H-CUSP schemes for turbomachinery applications, AIAA Paper 2003-4120-CP, in: 16th AIAA CFD Conference, June 2003.

[7] J.R. Edwards, M.-S. Liou, Low-diffusion flux-splitting methods for flows at all speeds, AIAA Journal 36 (1998) 1610–1617.

[8] M.-S. Liou, J.R. Edwards, Numerical speed of sound and its application to schemes for all speeds, AIAA Paper 99-3268-CP, in: 14th AIAA CFD Conference, 1999.

[9] M.-S. Liou, P.G. Buning, Contribution of the recent AUSM schemes to the OVERFLOW code: implementation and validation, AIAA Paper 2000-4404, 2000.

[10] I. Mary, P. Sagaut, M. Deville, An algorithm for unsteady viscous flows at all speeds, International Journal of Numerical Methods in Fluids 34 (2000) 371–401.

[11] J.R. Edwards, R.K. Franklin, M.-S. Liou, Low-diffusion flux-splitting methods for real fluid flows at all speeds, AIAA Journal 38 (2000) 1624–1633.

[12] J. Edwards, D. Mao, Development of low-diffusion flux-splitting methods for dense gas–solid flows, AIAA Paper 2001-2649-CP, 2001.

[13] H. Paillère, C. Core, J. Garcia, On the extension of the AUSM$^+$ scheme to compressible two-fluid models, Computers & Fluids 32 (2003) 891–916.

[14] C.-H. Chang, M.-S. Liou, A new approach to the simulation of compressible multifluid flows with AUSM$^+$ scheme, AIAA Paper 2003-4107, 2003.

[15] M.-S. Liou, C.J. Steffen Jr., A new flux splitting scheme, Journal of Computational Physics 107 (1993) 23–39. Also NASA TM 104404, May 1991.

[16] M.-S. Liou, A sequel to AUSM: AUSM$^+$, Journal of Computational Physics 129 (1996) 364–382. Also NASA TM 106524, March 1994.

[17] K.H. Kim, C. Kim, O. Rho, Methods for the accurate computations of hypersonic flows I. AUSMPW$^+$ scheme, Journal of Computational Physics 174 (2001) 38–80.

[18] B. Müller, Low mach number asymptotics of the Navier–Stokes equations and numerical implications, VKI CFD Lecture Series, 1999-03, 1999.

[19] R.G. Rehm, H.R. Baum, The equations of motion for thermally driven Buoyant flows, Journal of Research of the National Bureau of Standards 83 (1978) 297–308.
[20] M.-S. Liou, Ten years in the making–AUSM-family, AIAA Paper 2001-2521-CP, in: 15th AIAA CFD Conference, June 11–14, 2001.
[21] B. Van Leer, Flux-vector splitting for the Euler equations, Lecture Notes in Physics 170 (1982) 507–512.
[22] T.W. Roberts, The behavior of flux difference splitting schemes near slowly moving shock waves, Journal of Computational Physics 90 (1990) 141–160.
[23] S.K. Godunov, A difference method for the numerical calculation of discontinuous solutions of hydrodynamic equations, Mat. Sb 47 (1959) 271–306.
[24] B. Einfeldt, On Godunov-type methods for gas dynamics, SIAM Journal on Numerical Analysis 25 (1988) 294–318.
[25] Y. Wada, M.-S. Liou, An accurate and robust flux splitting scheme for shock and contact discontinuities, SIAM Journal on Scientific and Statistical Computing 18 (1997) 633–657.
[26] M.-S. Liou, Mass flux schemes and connection to shock instability, Journal of Computational Physics 160 (2000) 623–648.
[27] J.J. Quirk, A contribution to the great Riemann solver debate, International Journal of Numerical Methods Fluids 18 (1994) 555–574. Also ICASE Report 92-64, 1992.
[28] P.G. Buning, et. al., OVERFLOW User's Manual, version 1.8f, Unpublished NASA Report, 1998.
[29] R.V. Chima, Calculation of multistage turbomachinery using steady characteristic boundary conditions, AIAA Paper 98-0968. Also NASA TM-1998-206613, 1998.
[30] F.R. Mentor, Two-equation Eddy-viscosity turbulence models for engineering applications, AIAA Journal 32 (1994) 1598–1605.
[31] D.C. Wilcox, Reassessment of the scale-determining equation for advanced turbulence models, AIAA Journal 26 (1988) 1299–1310.
[32] P.R. Spalart, S.R. Allmaras, A one-equation turbulence model for aerodynamic flows, AIAA Paper 92-0439, 1992.
[33] B. Koren, Upwind schemes, multigrid and defect correction for the steady Navier–Stokes equations, Lecture Notes in Physics 323 (1989) 344–348.
[34] W.D. Bachalo, D.A. Johnson, Transonic turbulent boundary-layer separation generated on an axisymmetric flow model, AIAA Journal 24 (1986) 437–443.
[35] J. Vienrendeels, B. Merci, E. Dick, Blended AUSM$^+$ method for all speeds and all grid aspect ratios, AIAA Journal 39 (2001) 2278–2282.
[36] L.J. Goldman, R.G. Seasholtz, Laser anemometer measurements in an annular cascade of core turbine vanes and comparison with theory, NASA TP 2018, NASA Lewis Research Center, 1982.
[37] P.L. Johnson, K.M. Jones, M.D. Madson, Experimental investigation of a simplified 3D high lift configuration in support of CFD validation, AIAA Paper 2000-4217, 2000.
[38] A. Jameson, W. Schmidt, E. Turkel, Numerical solutions of the Euler equations by finite volume methods using Runge–Kutta time stepping, AIAA Paper 81-1259, 1981.
[39] D.A. Treadgold, A.F. Jones, K.H. Wilson, Pressure distribution measurement in the RA 8 ft × 6 ft transonic wind tunnel on RAE wing "A" in combination with an axi-symmetric body at mach numbers of 0.4, 0.8 and 0.9, Appendix B4, AGARD-AR-138, 1984.
[40] S.E. Rogers, K. Roth, S.M. Nash, CFD validation of high-lift flows with significant wind-tunnel effects, AIAA Paper 2000-4218-CP, in: AIAA 18th Applied Aerodynamics Conference, Denver, CO, 2000.